Energy Engineering

Tech Science Press

Doi:10.32604/ee.2025.072849

ARTICLE

Robust Optimal Scheduling of Integrated Energy Systems Considering Waste Heat Recovery from Power-to-Ammonia and Ammonia Cofiring Substitution

Xingzuo Pan[1], Yi Ding[2], Zhilong Wei[3], Tonglin Liu[4], Jianxin Ni[5] and Yupeng He[1,*]

[1]Department of Electrical Engineering, Northeast Electric Power University, Jilin, 132012, China
[2]Zhejiang Zheneng Zhongmei Zhoushan Coal Power Co., Ltd., Zhoushan, 316131, China
[3]CGN Cangnan Nuclear Power Co., Ltd., Wenzhou, 325800, China
[4]NARI RELAYS Electric Co., Ltd., Nanjing, 210000, China
[5]China Resources Power Xiantao Company, Xiantao, 433000, China

*Corresponding Author: Yupeng He. Email: 18943290602@163.com

Received: 04 September 2025; Accepted: 11 November 2025; Published: 27 May 2026

ABSTRACT: Wind and photovoltaic generation integration into power systems has steadily increased in recent years. To mitigate increasing renewable curtailment and deteriorating operational economics associated with high penetrations of wind and PV, this paper develops a robust optimal scheduling framework for integrated energy systems that integrates waste-heat recovery from power-to-ammonia (P2A) processes and ammonia cofiring as a substitution strategy. First, the energy transfer pathways of electricity–heat, ammonia, and the heat release characteristics of the entire P2A process are analyzed, enabling waste heat recovery throughout the conversion process. Second, considering the low-carbon characteristics of ammonia cofiring in gas turbine units, the combustion mechanism of ammonia–natural gas blends is examined. Subsequently, an energy-curtailment-driven carbon capture control strategy is developed by introducing electricity-heat flexible loads, and a collaborative operation model coupling carbon capture equipment with ammonia cofiring is constructed. Finally, a high-dimensional scenario set representing wind and photovoltaic fluctuations is generated via Latin hypercube sampling, clustered, and embedded into a two-stage distributionally robust optimization model. The proposed method is solved using the IBM solver, and simulation results verify its stability under extreme wind and photovoltaic volatility, achieving a 37.2% reduction in total cost and a 68.05% reduction in carbon emissions compared to the baseline scenario.

KEYWORDS: Power-to-ammonia; waste heat recovery; ammonia cofiring substitution; two stage robust optimization; curtailment driven carbon capture

1 Introduction

1.1 Background

Driven by the global carbon neutrality strategy, renewable energy sources represented by wind and Photovoltaic (PV) rapidly shift from supplementary to primary energy roles, becoming the main drivers of new electricity demand growth [1]. However, while large-scale integration of wind and PV promotes decarbonization of the energy mix, their inherent intermittency, variability, and reverse peak regulation characteristics have introduced multiple challenges to the system, including rising curtailment rates, insufficient reserve capacity, and deteriorating operational economics [2]. To overcome the bottleneck in renewable energy absorption, the international research community has focused on key technologies such as power to hydrogen storage, using cross-domain energy conversion to store surplus wind and PV generation [3].

Nevertheless, energy losses during hydrogen production and the high cost and risk associated with hydrogen storage and transport constrain their large-scale application [4]. Against this background, ammonia, because of its high energy density, low liquefaction/transportation costs, and carbon-free combustion, has been designated by many nations as a strategic energy carrier; consequently, proposals such as blending ammonia into coal combustion in existing coal plants aim to substitute traditional fossil fuels [5]. Although China has incorporated ammonia energy into guidelines for novel energy storage technologies, bottlenecks remain in coupling wind and PV-driven ammonia production, including insufficient consideration of renewable output uncertainty and unclear quantification of energy losses [6]. Therefore, constructing a multi-energy coupling mechanism that balances high absorption efficiency and low operating cost, while quantifying the dynamic impacts of wind and PV uncertainty on the system's low-carbon economic performance, has become a key issue for resolving deep renewable integration into the grid and is of great significance for advancing a secure and low-carbon transformation of the new power system.

1.2 Literature Survey

Wind and PV output are stochastic and intermittent, creating conflicts with power system supply–demand balance [7]. Electrolytic hydrogen production can convert renewable electricity into hydrogen for storage, and the hydrogen production process is near-zero carbon [8]; however, electrolytic hydrogen is constrained by high production costs and difficulties in hydrogen storage and transport. In this context, ammonia has emerged as a research focus because it is a flexible and low-cost energy carrier for storage and transport. Power to Ammonia (P2A) converts electricity into ammonia via synthesis following electrolysis, addressing the hydrogen storage and transport challenge and providing a practical pathway for large-scale renewable energy storage. Reference [9] demonstrated the efficiency advantages and low carbon characteristics of P2A relative to fossil fuels. Reference [10] integrated P2A with liquid air energy storage to form an ammonia power cogeneration system capable of mitigating power supply and demand uncertainty. Reference [11] analyzed the economic low-carbon benefits and energy consumption levels of ammonia storage and combustion. Reference [12] proposed a low-carbon economic optimal scheduling model that jointly operates oxyfuel combustion and P2A. Reference [13] performed thermodynamic modeling of the P2A electrolysis process and translated long-term degradation into short-term cost terms. However, the above studies treat P2A as a monolithic system and do not implement modular or detailed modeling, which hampers accurate quantification of internal energy flow coupling mechanisms and dynamic constraints within the P2A system, and fails to expose the cascading loss effects of renewable fluctuations on ammonia conversion efficiency.

As a hub for coupling electricity, heat, and chemical energy, green ammonia enables large-scale production to supply low-carbon fuel for coal-fired units and simultaneously serves as a fuel substitute and an energy storage medium. In contrast, ammonia cofiring can achieve low-cost coal-fired units transformation without extensive equipment retrofits [14]. Reference [15] analyzed key technologies and combustion kinetics of ammonia and discussed how ammonia cofiring contributes to low-carbon goals. Reference [16] examined ammonia fuel characteristics and validated the feasibility of ammonia cofiring. Reference [17] demonstrated the potential for carbon emission reduction via ammonia cofiring in boiler systems. Reference [18] reviewed application prospects and development trends for ammonia fuel and identified ammonia cofiring as an important decarbonization pathway. Reference [19] employed curtailed wind power to drive P2A production of green ammonia to reduce system carbon emissions and enhance renewable absorption. Reference [20] proposed a two-layer optimization model based on P2A carbon capture coordination and ammonia cofiring to improve renewable absorption and low-carbon economic operation. Nevertheless, these studies mainly

focus on emission reduction and absorption capability of ammonia cofiring and do not consider the synergistic benefits of green ammonia deployment and curtailed energy-driven carbon capture for decarbonization and renewable absorption. Moreover, the high-temperature waste heat recovery from ammonia synthesis during green ammonia production and the dynamic matching with electricity and heat demand response (DR) have not been adequately addressed, leaving substantial potential for improving overall system energy efficiency unexplored.

Ammonia cofiring as a fuel substitution alleviates the energy supply conflict and carbon emission pressure of carbon capture-equipped units; however, under scenarios with high PV and wind penetration, the output variability of these resources can still induce electricity to ammonia supply and demand imbalances within the P2A system. Existing research predominantly relies on stochastic programming and robust optimization approaches to handle uncertainties in integrated energy systems (IES) [21]. Reference [22], for an IES with ammonia storage, quantifies wind and PV stochastic fluctuations using joint probability distributions and constructs a coordinated representation model for multi-source uncertainty, mitigating adverse impacts on economic performance and low-carbon targets. Reference [23] represents renewable generation (RG) variability using uncertainty sets and develops a two-stage robust optimization formulation for IES with P2A to ensure feasibility under severe fluctuations. Nevertheless, faced with the high-dimensional and substantial uncertainty of wind and PV, stochastic programming becomes increasingly difficult to formulate, and conventional robust optimization struggles to finely capture the spatiotemporal correlation characteristics of renewable output and their complex impacts on the coupling of electricity and ammonia energy flows. Reference [24] extracts representative scenario features through scenario generation and clustering to accurately characterize multiple wind PV and load uncertainties for production planning optimization. Despite progress in scenario generation and robust optimization, these works have not clarified the intrinsic coupling between the two approaches in P2A systems, which leads to scheduling solutions that diverge from low-carbon economic optima and impedes the simultaneous optimization of ammonia-dispatch robustness and the economic performance of ammonia synthesis under multiple sources of variability.

1.3 Research Gap

Although prior studies have made pioneering contributions, several research gaps remain:

1. Existing models often treat power-to-ammonia (P2A) as a 'black-box' unit, neglecting critical processes such as electrolyzer start-stop delays and the recovery of reaction heat from ammonia synthesis. This oversight results in the inefficient utilization of thermal energy generated during water electrolysis and the ammonia production stage, leading to a loss of energy cascade utilization efficiency.
2. Current research fails to consider the synergistic carbon reduction potential between green ammonia fuel supply and carbon capture driven by curtailed renewable energy. Consequently, the collaborative benefits of green ammonia applications and carbon capture in enhancing renewable energy consumption remain unexplored. Furthermore, the failure to align these strategies with the dynamic characteristics of IDR restricts the potential for optimized energy utilization.
3. Existing scheduling studies of systems incorporating P2A rely solely on scenario generation techniques to represent uncertainty or employ robust optimization to handle extreme scenarios. This approach leads to an imprecise quantification of the electricity-ammonia supply-demand imbalance risk triggered by fluctuating wind and solar power within the robust framework. Consequently, there is significant room for improvement in identifying the optimal solution for generating units' low-carbon and economic dispatch.

1.4 Contribution

This study develops a robust optimal scheduling approach for IES that incorporates P2A waste-heat recovery and ammonia cofiring as a substitution measure. The main contributions are as follows:

1. A novel modular modeling framework for the complete P2A production chain is developed, which explicitly captures the high-grade waste heat (350°C–380°C) generated during the exothermic ammonia synthesis reaction. This heat is recovered through a dedicated waste heat boiler (WHB) system and dynamically allocated to either direct thermal load supply or thermal energy storage, enabling cascade utilization of thermal energy across electricity, heat, and chemical domains. This represents a significant advancement over existing "black-box" P2A models and provides a foundation for efficient renewable-driven ammonia production with enhanced energy integration.
2. An innovative curtailment-driven carbon capture strategy is proposed, where the CCPP operates exclusively on surplus renewable energy. Furthermore, we establish a synergistic mechanism between green ammonia supply and carbon capture, where waste heat from ammonia synthesis partially supports the capture process, creating a closed-loop carbon-energy nexus. This coordination significantly enhances both renewable energy utilization and system-wide decarbonization.
3. A scenario generation and robust optimization coordinated framework is adopted, whereby a high-dimensional scenario set of wind and PV fluctuations is produced and clustered, then embedded into a two-stage distributionally robust optimization model. This framework precisely transmits the impacts of renewable variability to ammonia supply and demand, enabling the system to maintain low-carbon economic operation under high-dimensional uncertainty.

2 IES Model Formulation with P2A Waste Heat Recovery and Ammonia Substitution

The refined electricity–heat–ammonia IES developed in this study is depicted in Fig. 1 and comprises a hydrogen production unit, a detailed P2A facility, and a power plant equipped with carbon capture, achieving efficient low-carbon operation via coordinated conversion across multiple energy vectors.

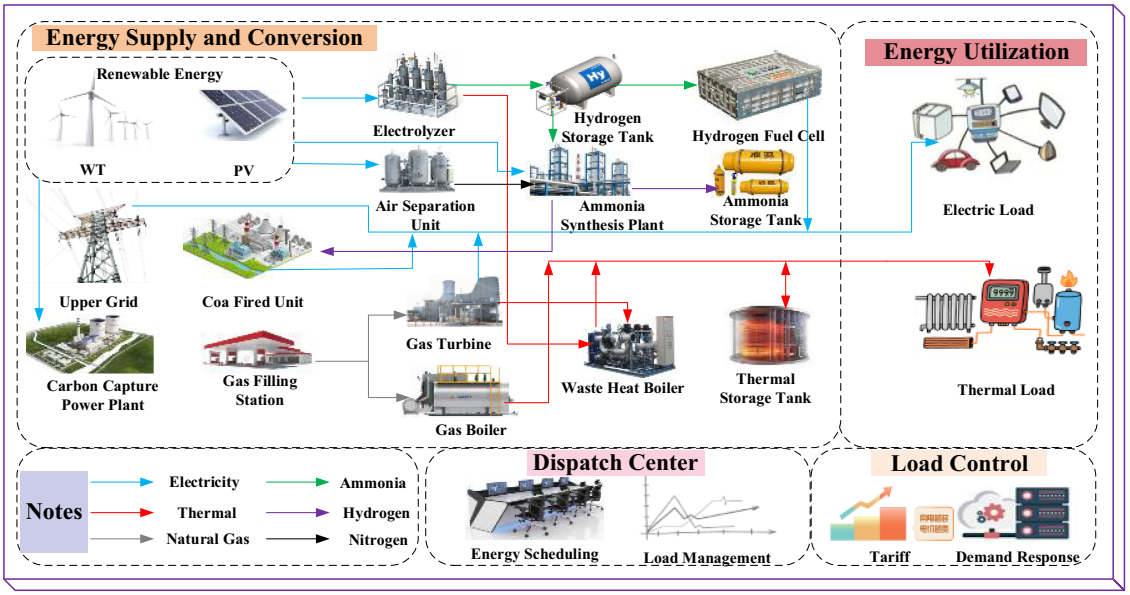

Figure 1: Structure diagram of the IES

In the system, electrical demand is jointly supplied by wind farms, PV, coal-fired units, hydrogen fuel cells, and gas turbines (GT); thermal demand is met by gas boilers (GB), waste heat recovery from GT, and process heat from the P2A plant. The hydrogen unit and the P2A facility are tightly coupled to enable multi-directional conversion and storage among electricity, heat, hydrogen, and ammonia. The energy consumption of the CCPP is supplied by renewable sources and, acting as a flexible controllable load, participates in system power balancing and renewable absorption.

During abundant wind and PV output coupled with low electric load, surplus electricity drives the electrolyzer to produce hydrogen, which supplies hydrogen fuel cells for storage and the ammonia synthesis process. Waste heat generated during ammonia synthesis is recovered via heat exchangers and directly supplied to thermal loads or storage units. In periods of insufficient wind and PV output and peak electric load, hydrogen stored in hydrogen tanks is converted to electricity by hydrogen fuel cells. In contrast, liquid ammonia stored in ammonia tanks is cofired with or substitutes for coal in thermal power units to jointly alleviate power deficits in the grid. Meanwhile, waste heat from the electrolyzer and ammonia synthesis continues to meet thermal demand. The CCPP operates flexibly according to system net load and carbon constraints, enhancing renewable energy absorption capability.

The detailed process of the refined P2A facility is illustrated in Fig. 2. The model comprehensively characterizes the key stages of ammonia synthesis, including water electrolysis for hydrogen production, air separation for nitrogen generation, and ammonia synthesis from nitrogen and hydrogen, as well as the dynamic characteristics of core unit equipment such as compressors, heat exchangers, ammonia reactors, refrigeration systems, and separation devices. Under catalytic action, nitrogen and hydrogen undergo highly exothermic thermodynamic reactions to form ammonia. The reaction products are cooled and liquefied by the refrigeration system, then purified into liquid ammonia via high and medium-pressure separation units. The model finely captures the gas circulation control process: unreacted nitrogen-hydrogen mixed gas is recycled through vent pipes back into the system for further reaction, while inert gases accumulated in the synthesis loop are vented.

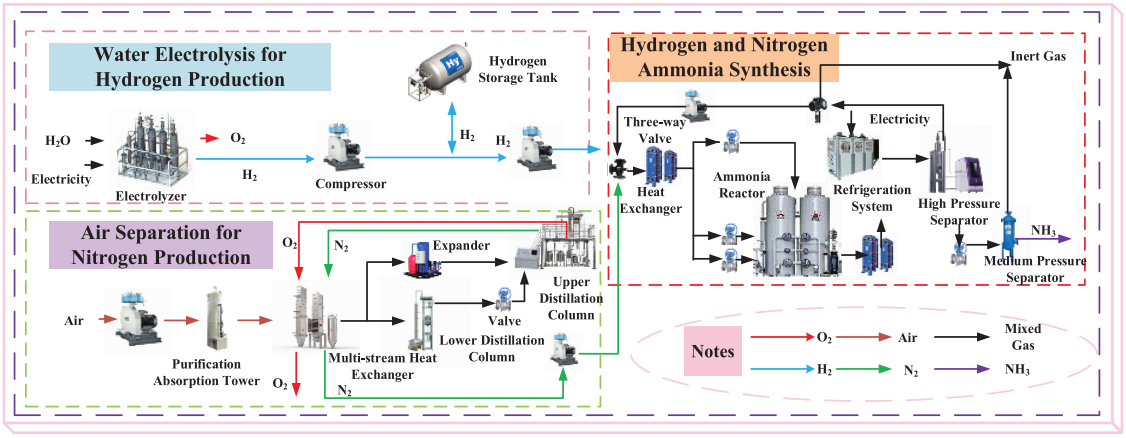

Figure 2: Detailed structure of P2A production

2.1 Water Electrolysis Module

The renewable energy hydrogen production system adopts an AEL, with the reactions as follows [25]:

$$H_2O \rightarrow H_2 + \frac{1}{2}O_2 \tag{1}$$

Anode:

$$2OH^- \rightarrow \frac{1}{2}O_2 + H_2O + 2e^- \tag{2}$$

Cathode:

$$2H_2O + 2e^- \rightarrow H_2 + 2OH^- \tag{3}$$

This study focuses on the role of the electrolyzer in accommodating renewable energy, setting the electrolyzer efficiency as a fixed parameter. The operation model of the hydrogen unit can be expressed as:

$$\begin{cases} M_t^{H_2} = \dfrac{\eta^{H_2} P_t^{H_2}}{\delta^{H_2}} \\ M_t^{\mathrm{HST}} = M_{t-1}^{\mathrm{HST}} + \eta_{\mathrm{HST}}^{\mathrm{in}} M_t^{H_2} - \dfrac{M_t^{H_2,\mathrm{gt}}}{\eta_{\mathrm{HST}}^{\mathrm{out}}} \end{cases} \tag{4}$$

where $M_t^{\mathrm{H_2}}$ is the hydrogen mass produced by the electrolyzer; $P_t^{\mathrm{H_2}}$ is the energy consumption of the electrolyzer; η^{H_2}, δ^{H_2} represents the electrolyzer's operating efficiency and electricity-to-hydrogen conversion coefficient; M_t^{HST}, M_{t-1}^{HST} denotes the hydrogen storage in the hydrogen tank; $\eta_{\mathrm{HST}}^{\mathrm{in}}$, $\eta_{\mathrm{HST}}^{\mathrm{out}}$ indicates the hydrogen charging and discharging efficiencies of the storage tank.

2.2 Hydrogen Fuel Cell Module

This study establishes a control model founded on the combined-heat-and-power characteristics of hydrogen fuel cells. The operational model is given by Eq. (5).

$$\begin{cases} P_t^{\mathrm{HFC}} = \eta_{t,e}^{HFC} M_{t,H_2}^{\mathrm{HFC}} \\ Q_t^{\mathrm{HFC}} = \eta_{t,h}^{HFC} M_{t,H_2}^{\mathrm{HFC}} \end{cases} \tag{5}$$

where M_{t,H_2}^{HFC} is the hydrogen mass input to the fuel cell; P_t^{HFC}, Q_t^{HFC} are the electrical and thermal power outputs; $\eta_{t,e}^{HFC}$, $\eta_{t,h}^{HFC}$ represent the electrical and thermal efficiencies of the fuel cell.

2.3 Air Separation Nitrogen Production Module

Part of the electricity generated by wind and PV is supplied to the Air Separation Unit (ASU), which separates nitrogen and oxygen through cryogenic distillation, exploiting their boiling point difference [26]. The model is expressed by Eq. (6).

$$\begin{cases} Q_{\mathrm{N_2}} = Q_{\mathrm{air}} \cdot y_{\mathrm{N_2}} \cdot \eta_{\mathrm{sep}} \\ \eta_{\mathrm{sep}} = \eta_{\max} \cdot \left[1 - e^{-k_p \cdot (P_{\mathrm{DC}} - P_{\min})}\right] \\ W_{\mathrm{comp}} = \dfrac{Q_{\mathrm{air}} \cdot R \cdot T_1}{\eta_{\mathrm{comp}}} \left[\left(\dfrac{P_{\mathrm{DC}}}{P_1} \right)^{\frac{\gamma-1}{\gamma}} - 1 \right] \\ E_{\mathrm{ASU}} = W_{\mathrm{comp}} + Q_{\mathrm{air}} \cdot c_p \cdot (T_1 - T_{\mathrm{L}}) \end{cases} \tag{6}$$

where $Q_{\mathrm{N_2}}$ is the nitrogen production; Q_{air} is the air inlet flow rate; P_{DC} is the operating pressure of the distillation column; $P_{\min}$ is the minimum liquefaction pressure; T_L is the liquefaction temperature; T_1 is the compressor inlet temperature; η_{sep} is the air separation efficiency; η_{comp} is the compressor efficiency; $\eta_{\max}$ is the maximum separation efficiency; W_{comp} is the compressor power consumption; k_p is the pressure influence coefficient; c_p is the specific heat capacity of air at constant pressure; E_{ASU} is the total energy consumption of the air separation unit for nitrogen production.

2.4 Nitrogen Synthesis Unit Modeling

This study employs the mature Haber-Bosch (H-B) process for ammonia synthesis, as illustrated in Fig. 3.

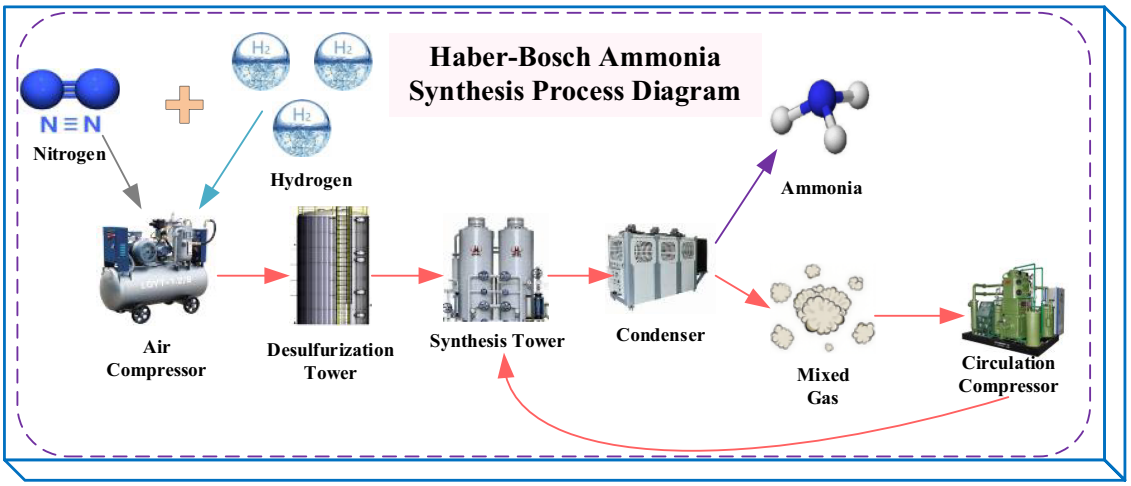

Figure 3: Haber-Bosch ammonia synthesis process diagram

The process uses hydrogen produced via water electrolysis and nitrogen from the ASU as feed gases. Ammonia is synthesized at elevated temperature and pressure, subsequently cooled and separated to yield liquid ammonia; the reaction is shown in Eq. (7).

$$N_2 + 3H_2 \rightleftharpoons 2NH_3 \tag{7}$$

To ensure production safety and comply with thermodynamic balance and catalyst activity constraints, the ammonia yield in the synthesis unit must be maintained within specified limits. Its rate of change and ramping speed must satisfy upper and lower bound constraints [27].

$$\begin{cases} m_t^{NH_3} = m_{t-1}^{NH_3} + r_t^{NH_3} \\ r_{\min^{NH_3}} \le r_t^{NH_3} \le r_{\max^{NH_3}} \\ m_{\min^{NH_3}} \le m_t^{NH_3} \le m_{\max^{NH_3}} \\ P_t^{NH_3} = c^{NH_3} m_t^{NH_3} \end{cases} \tag{8}$$

where $m_t^{NH_3}$ is the ammonia yield, $r_t^{NH_3}$ is the ammonia yield ramp rate; $m_{\max}^{NH_3}$ and $m_{\min}^{NH_3}$ are the lower and upper limits of the ramp rate; $r_{\max^{NH_3}}$ and $r_{\min^{NH_3}}$ are the lower and upper limits of ammonia yield; $P_t^{NH_3}$ is the energy consumption of the synthesis unit; c^{NH_3} is the electricity consumption per unit mass of ammonia produced.

2.5 Waste Heat Recovery and Power Generation Unit

The waste heat recovery process represents a key innovation in our P2A modeling approach. As shown in Fig. 4, the high-temperature reaction gas (350°C–380°C) exiting the ammonia synthesis tower passes through a waste heat boiler (WHB), where it is cooled to 240°C–250°C. This temperature reduction enables the recovery of substantial high-grade thermal energy.

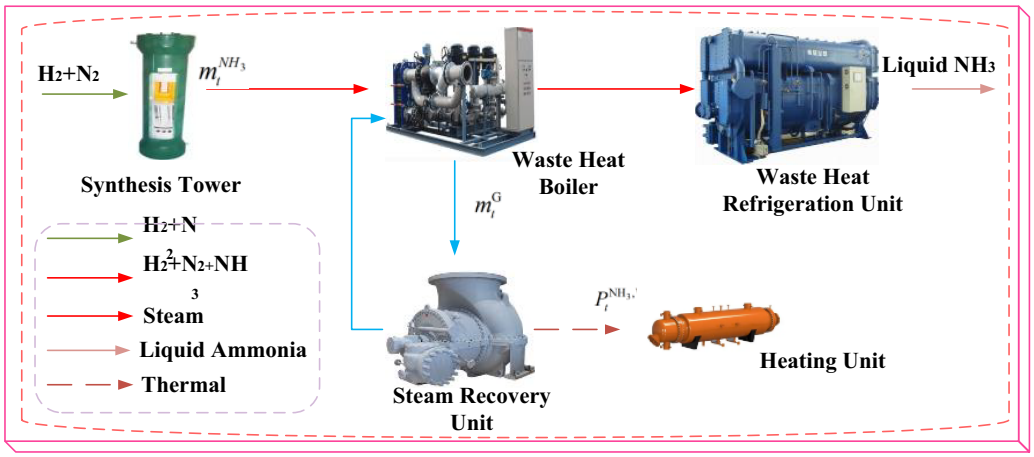

Figure 4: Waste heat unit diagram

The recovered heat is utilized through multiple pathways:

Direct thermal supply: Generated high-pressure steam directly serves thermal loads.

Thermal energy storage: Excess heat is stored in thermal storage tanks for time-shifted utilization.

Carbon capture support: Partial heat supply to the carbon capture system's regeneration process.

This multi-level utilization strategy enables cascade energy recovery from the exothermic ammonia synthesis reaction, significantly enhancing overall system efficiency. The thermal power recovered by the WHB is modeled as:

$$\begin{cases} Q_t^{\mathrm{NH_3,WH}} = M_{\mathrm{A}} m_t^{\mathrm{NH_3}} C_{\mathrm{p}} \left(T_1 - T_2\right) \\ m_t^{\mathrm{G}} = \left(1 - \eta_{\mathrm{sun}}\right) \left[Q_t^{\mathrm{NH_3,WH}} / \left(H_1 - H_2\right)\right] \\ P_t^{\mathrm{NH_3,WH}} = m_t^{\mathrm{G}} H_1 \\ Q_{WHB,t} = \dot{m}_{NH3,out} \cdot c_p \cdot \left(T_{in} - T_{out}\right) \cdot \eta_{WHB} \end{cases} \tag{9}$$

where $Q_t^{\mathrm{NH_3,WH}}$ is the heat recovered by the waste heat boiler; $m_t^{\mathrm{NH_3}}$ is the ammonia production rate; M_{A} is the average flow rate of the ammonia synthesis tower outlet gas per unit mass of ammonia produced; C_{p} is the average specific heat capacity of the ammonia synthesis tower outlet gas; T_1 is the average inlet temperature of the waste heat boiler gas; T_2 is the average outlet temperature of the waste heat boiler gas; m_t^{G} is the byproduct steam produced by the waste heat boiler; η_{sun} is the heat loss rate of the waste heat boiler; H_1 is the enthalpy of high pressure steam generated by the waste heat boiler; H_2 is the enthalpy of boiler water in the waste heat boiler; $P_t^{\mathrm{NH_3,WH}}$ is the heat output power of the waste heat unit. $\dot{m}_{NH3,out}$ represents the mass flow rate of synthesis gas, c_p denotes specific heat capacity, T_{in} and T_{out} are inlet and outlet temperatures, respectively, and η_{WHB} is the heat recovery efficiency.

2.6 Coal-Fired Unit Ammonia Cofiring Model

Ammonia possesses a calorific value comparable to coal; consequently, cofiring ammonia in coal-fired units can reduce coal consumption. The ammonia cofiring technology involves mixing ammonia gas into the existing pulverized coal combustion process, as shown in Fig. 5.

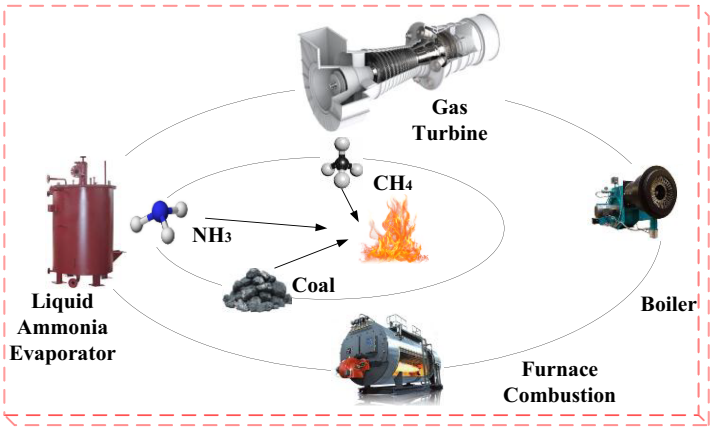

Figure 5: Ammonia cofiring schematic

The operation model of ammonia cofiring in coal-fired units is expressed as [20]:

$$\begin{cases} M_{i,t}^{\text{coal,NH}_3} = a_i \left(P_{i,t}^{\text{TP}}\right)^2 + b_i P_{i,t}^{\text{TP}} + c_i - m_t^{\text{NH}_3} \dfrac{Q_{\text{NH}_3}}{Q_{\text{coal}}} \\ M_{i,t}^{\text{coal}} = a_i \left(P_{i,t}^{\text{TP}}\right)^2 + b_i P_{i,t}^{\text{TP}} + c_i \\ \zeta_t = \dfrac{m_t^{\text{NH}_3} Q_{\text{NH}_3}}{M_{i,t}^{\text{coal,NH}_3} Q_{\text{coal}}} \end{cases} \tag{10}$$

where a_i, b_i, c_i are the coal consumption characteristic coefficients; $M_{i,t}^{\text{coal,NH}_3}$, $M_{i,t}^{\text{coal}}$ represent the coal consumption of unit i during time period t with and without ammonia cofiring; $P_{i,t}^{\text{TP}}$ is the power output of unit i; Q_{NH_3}, Q_{coal} denote the lower heating values of ammonia and coal; $m_t^{\text{NH}_3}$, ζ_t are the ammonia quantity and ammonia blending ratio of the coal-fired unit.

2.7 Carbon Capture Power Plant Model

The CCPP in this study is fully powered by curtailed wind and PV energy and operates under a flexible scheduling strategy: it runs only when renewable generation exceeds the grid's baseload demand, serving as a controllable load to absorb renewable variability and intermittency. Its structure is shown in Fig. 6. The CCPP model is given by Eq. (11) [28]:

$$\begin{cases} P_t^{CCS} = P_{r,t}^{CCS} + P_{s,t}^{CCS} \\ P_{r,t}^{CCS} = \lambda_{\text{GE}} \eta_{\text{C}} P_t^G \\ E_{\text{t}}^{CC} = \eta_{\text{C}} e_{\text{G}} P_t^G \\ 0 \leqslant P_t^{CCS} \leqslant P_{\text{CCS}}^{\max} \end{cases} \tag{11}$$

where P_t^{CCS} is the total power of the CCS; $P_{r,t}^{CCS}$ is the operating energy consumption of the CCS; $P_{s,t}^{CCS}$ is the fixed energy consumption of the CCS, considered constant; P_t^G is the generation power of wind or PV units; η_{C} is the carbon capture efficiency of the CCS; λGE is the electrical power consumption per unit of CO_2 captured; $P_{\text{CCS}}^{\max}$ is the upper limit of CCS operating power.

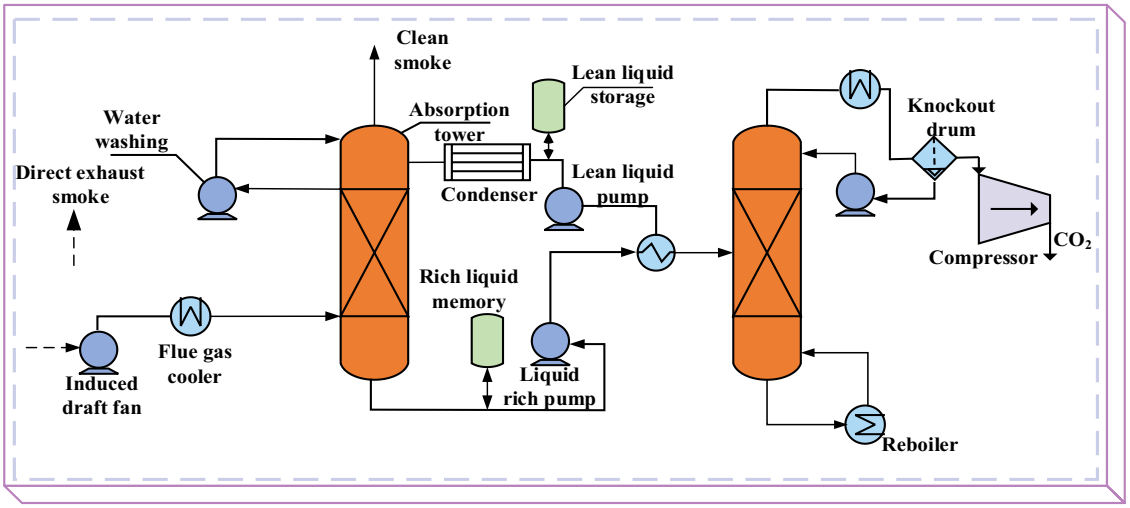

Figure 6: CCPP structure

Given the substantial energy demand of carbon capture, this study adopts a CCPP configuration with a flue-gas bypass to enable controlled CO_2 venting and thus limit capture energy use. The corresponding expression is as follows:

$$E_1(t) = E(t) - e_1(t) \tag{12}$$

where $E(t)$ and $E_1(t)$ represent the total emissions and CO_2 absorbed by the CCS; $e_1(t)$ is the amount of CO_2 released to the atmosphere via flue gas bypass.

It is important to note that the proposed flexible operation strategy for the CCPP, while reducing its annual utilization rate, is economically justified within the context of this study under two key premises: First, the primary energy input for the capture process is *curtailed* renewable electricity, which has a near-zero marginal cost. This eliminates conventional carbon capture systems' most significant operational expenditure (OPEX) component. Second, the stepwise carbon trading mechanism imposes significantly higher penalties as emissions increase. The CCPP is a strategic asset to avoid these punitive carbon costs at the system level. The model optimizes for overall system cost, which includes carbon trading expenses, rather than maximizing the standalone revenue of the CCPP. The capture equipment's capital expenditure (CAPEX) is assumed to be justified by the aggregated value it provides through carbon cost savings and enhanced renewable energy utilization across the entire IES.

2.8 Stepwise Carbon Trading Mechanism Model

This study develops a stepwise carbon trading mechanism based on conventional carbon trading. Fig. 7 illustrates the stepwise carbon trading mechanism.

System carbon emission allowances are determined using the baseline method; the model is given by Eq. (13):

$$E_q = \sum_{t}^{T} \left(\delta_{\text{grid}} P_t^{\text{buy}} + \delta_{\text{MT}} P_t^{\text{MT}} + \delta_{\text{GB}} P_{\text{h},t}^{\text{GB}} \right) \tag{13}$$

where E_q is the total carbon emission allowance allocated to the HIES, δ is the carbon allowance per unit generation of emitting units (t/MWh), P_t^{buy} is the system electricity purchase (MW).

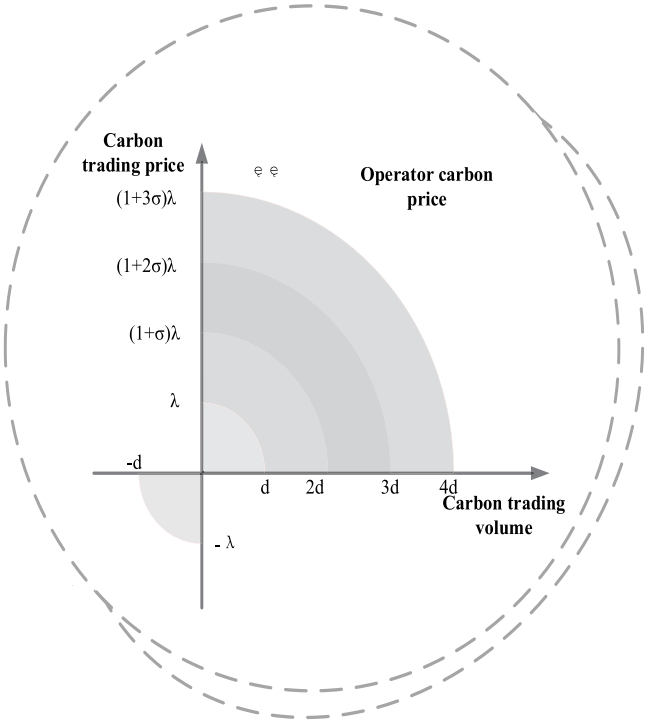

Figure 7: Stepwise carbon trading mechanism diagram

System carbon emissions primarily originate from GT, GB, and coal-fired units. The carbon trading cost is expressed as follows [29]:

$$C_{CO_2} = \begin{cases} \lambda\left(E_a - E_q\right), 0 < E_a - E_q \le l \\ \lambda l + \lambda\left(1+\mu\right)\left(E_a - E_q - l\right), \\ \qquad l < E_a - E_q \le 2l \\ \lambda\left(2+\mu\right) l + \lambda\left(1+2\mu\right)\left(E_a - E_q - 2l\right), \\ \qquad 2l < E_a - E_q \le 3l \\ \lambda\left(3+3\mu\right) l + \lambda\left(1+3\mu\right)\left(E_a - E_q - 3l\right), \\ \qquad 3l < E_a - E_q \end{cases} \tag{14}$$

where E_a is the system's actual carbon emissions; λ is the base carbon price in the carbon trading market (¥/kg); μ is the growth rate of carbon trading price across different tiers; l is the length of the carbon emission interval. Fig. 7 illustrates the stepwise carbon trading mechanism.

2.9 Electric and Thermal Load DR Model

Adjustable electrical loads include time-shiftable loads and interruptible loads [30]:

$$\begin{cases} P_t^L = P_t^{L0} + P_t^{TSL} - P_t^{IL} \\ P_{\min}^{TSL} \le P_t^{TSL} \le P_{\max}^{TSL} \\ \sum_{t=1}^{T} P_t^{TSL} = 0 \\ 0 \le P_t^{IL} \le P_{\max}^{IL} \end{cases} \tag{15}$$

where P_t^{L0} is the electrical load before demand response; P_t^L is the electrical load after demand response; P_t^{TSL} is the shiftable electrical load; P_t^{IL} is the interruptible electrical load; $P_{\max}^{TSL}$, $P_{\min}^{TSL}$ are the upper and lower bounds of shiftable electrical load; $P_{\max}^{IL}$ is the upper bound of interruptible electrical load.

Adjustable thermal loads comprise interruptible loads and time-shiftable loads [31]:

$$\begin{cases} \Delta Q_{\text{int},t} = \Delta Q_{\text{int,max},t} \cdot \gamma_{\text{temp},t} \cdot (1 - \kappa_{\text{comf},t}) \\ \sum_{t=1}^{T} Q_{\text{shift},t} = \sum_{t=1}^{T} Q_{\text{shift},t}^0 \\ Q_{\text{shift},t}^{\min} \le Q_{\text{shift},t} \le Q_{\text{shift},t}^{\max} \\ \Delta Q_t = \Delta Q_{\text{int},t} + \left| Q_{\text{shift},t} - Q_{\text{shift},t}^0 \right| \end{cases} \tag{16}$$

where $\Delta Q_{\text{int},t}$ is the actual reduction of interruptible thermal load; $\Delta Q_{\text{int,max},t}$ is the maximum theoretical interruptible amount; $\gamma_{\text{temp},t}$ is the temperature influence coefficient; $\kappa_{\text{comf},t}$ is the comfort discount coefficient (range $0 \le \kappa_{\text{comf},t} < 0.3$, ensuring temperature adjustments remain within human tolerance). $Q_{\text{shift},t}$ is the thermal load power after shifting; $Q_{\text{shift},t}^0$ is the original thermal load power; $Q_{\text{shift},t}^{\min}$ and $Q_{\text{shift},t}^{\max}$ are the lower and upper bounds, respectively, of allowable load shifting. The total adjustable thermal load response in period t, denoted ΔQ_t, is composed of interruptible and shiftable loads.

3 Robust Optimization of IES with P2A Waste Heat Recovery and Ammonia Cofiring Substitution

3.1 Two-Stage Robust Optimization Model

Robust optimization typically employs uncertainty sets to describe the uncertainty of wind and PV output [32–34]. In this study, uncertainty sets are used for wind PV and load. The variability of designated uncertain variables may be written as follows:

Wind uncertainty set:

$$\begin{cases} P_{e,WT,t}^* = P_{e,WT,t} + z_{WT,t}^+ \Delta P_{e,WT,t}^+ - z_{WT,t}^- \Delta P_{e,WT,t}^- \\ z_{WT,t}^+ + z_{WT,t}^- \le 1 \\ \sum_{t=1}^{T} \left(z_{WT,t}^+ + z_{WT,t}^- \right) \le \Gamma_{WT} \end{cases} \tag{17}$$

where $P_{e,WT,t}^*$ denotes the available electrical power of the wind turbine (WT); $\Delta P_{e,WT,t}^+$ and $\Delta P_{e,WT,t}^-$ denote the upward and downward regulation power of WT; $z_{WT,t}^+$ and $z_{WT,t}^-$ denote the upward and downward regulation status variables of WT, represented as binary 0 1 variables; Γ_{WT} denotes the fluctuation parameter of WT uncertainty.

PV uncertainty set:

$$\begin{cases} P^{*}_{e,PV,t} = P_{e,PV,t} + z^{+}_{PV,t}\Delta P^{+}_{e,PV,t} - z^{-}_{PV,t}\Delta P^{-}_{e,PV,t} \\ z^{+}_{PV,t} + z^{-}_{PV,t} \le 1 \\ \sum_{t=1}^{T}\left(z^{+}_{PV,t} + z^{-}_{PV,t}\right) \le \Gamma_{PV} \end{cases} \tag{18}$$

where $P^{*}_{e,PV,t}$ denotes the available PV electrical power; $\Delta P^{+}_{e,PV,t}$ and $\Delta P^{-}_{e,PV,t}$ denote the upward and downward regulation power of PV; $z^{+}_{PV,t}$ and $z^{-}_{PV,t}$ denote the upward and downward regulation status variables of PV, represented as binary 0 1 variables; Γ_{PV} denotes the fluctuation parameter of PV uncertainty.

Electric load uncertainty set:

$$\begin{cases} P^{*}_{e,L,t} = P_{e,L,t} + z^{+}_{L,t}\Delta P^{+}_{e,L,t} - z^{-}_{L,t}\Delta P^{-}_{e,L,t} \\ z^{+}_{L,t} + z^{-}_{L,t} \le 1 \\ \sum_{t=1}^{T}\left(z^{+}_{L,t} + z^{-}_{L,t}\right) \le \Gamma_{L} \end{cases} \tag{19}$$

where $P_{e,L,t}$ denotes the baseline electrical load power; $\Delta P^{+}_{e,L,t}$ and $\Delta P^{-}_{e,L,t}$ denote the allowable upward and downward adjustment magnitudes of the electrical load; $z^{+}_{L,t}$ and $z^{-}_{L,t}$ are binary decision variables (0, 1) indicating whether upward or downward adjustment is enabled; Γ_{L} is the uncertainty budget parameter for electrical load, which limits the total number of adjustments and controls the conservativeness of the model.

Thermal load uncertainty set:

$$\begin{cases} Q^{*}_{h,L,t} = Q_{h,L,t} + w^{+}_{L,t}\Delta Q^{+}_{h,L,t} - w^{-}_{L,t}\Delta Q^{-}_{h,L,t} \\ w^{+}_{L,t} + w^{-}_{L,t} \le 1 \\ \sum_{t=1}^{T}\left(w^{+}_{L,t} + w^{-}_{L,t}\right) \le \Gamma_{L,h} \end{cases} \tag{20}$$

where $Q_{h,L,t}$ denotes the baseline thermal load power; $\Delta Q^{+}_{h,L,t}$ and $\Delta Q^{-}_{h,L,t}$ denote the allowable upward and downward adjustment amounts of the thermal load; $w^{+}_{L,t}$ and $w^{-}_{L,t}$ are binary state variables for thermal load, independent of electrical load decisions; $\Gamma_{L,h}$ is the thermal load uncertainty fluctuation parameter.

The optimization separates the binary startup and shutdown decisions from the continuous output decisions [35]. In the first stage, startup and shutdown decisions for units are determined. After these decisions are fixed, they are passed to the second stage, which accounts for uncertain parameters and derives the optimal solution under worst-case conditions [36]. The standard form of the Two Stage Robust Optimization model for the IES is:

$$\begin{cases} \min_{y} c^{T}y + maxmin\left(b^{T}x + d^{T}x^{2}\right) \\ u \in U, X \in T\left(y,u\right) \\ Dy \ge \mathrm{e}, Fx \ge \mathrm{f}, \quad Ex \ge 0 \\ Lx + Ny \ge 0, Gx = \mathrm{g} \\ Hx = u, Jx + Ky = 0 \end{cases} \tag{21}$$

where x is the column vector of all unit output decision variables for the IES; x^{2} is the column vector of the squares of all unit output decision variables; y is the column vector of all unit start up and shutdown decision

variables; $T(y, u)$ denotes the feasible region of second stage decision variables x when first stage decisions y and uncertain parameters u are fixed.; *b, c, d* are column vectors of cost coefficients for the IES units; *D, E, F, G, H, L, N, J, K* are the constraint coefficient matrices for all decision variables in the IES; e, f, g are constant column vectors.

3.2 Objective Function

This study minimizes the aggregate of energy purchase/sale costs, equipment operating expenses, electrolyzer startup and shutdown costs, and other related expenditures, while explicitly modeling uncertainties associated with wind, PV, and load. A two-stage distributionally robust optimization model for renewable-driven ammonia production is formulated. Within this two-stage robust optimization framework, ambiguity sets for uncertainty distributions are constructed using composite norms (i.e., the infinity norm and the one-norm) to characterize system variability.

The first stage solves a minimization problem whose primary purpose is to obtain the cost-minimizing scheduling plan under a given probability distribution of renewable scenarios. The second stage solves a max-min problem that searches for the probability distribution that maximizes system operating cost. The worst-case renewable scenario distribution, expressed as:

$$
\begin{aligned}
&C_{\mathrm{IES,BiRO}} = \max_{u=U} \min C_{\mathrm{IES}} \\
&\min C_{\mathrm{IES}} = C_A + C_B + C_C + C_D + C_E + C_{CO2} + C_{CT} \\
&C_A = \sum_{t=1}^{T} \left(W_{\mathrm{gas,price},t} \left(F_{\mathrm{gas},GT,t} + F_{\mathrm{gas},GB,t} \right) + W_{\mathrm{coal,price}} F_{\mathrm{coal},t} + W_{\mathrm{electricity,price},t} P_{e,\mathrm{buy},t} \right) \\
&C_B = \sum_{t=1}^{T} \left(\eta_{ab,WT} P_{ab,WT,t} + \eta_{ab,PV} P_{ab,PV,t} \right) \\
&C_C = \sum_{t=1}^{T} \left(\beta_{WT} P_{e,WT,t} + \beta_{PV} P_{e,PV,t} + \beta_{GT} P_{e,GT,t} + \beta_{GB} P_{e,GB,t} + \beta_{\mathrm{coal}} P_{e,\mathrm{coal},t} \right) \\
&C_D = \sum_{t=1}^{T} \left(\alpha_{GT,t} C_{\text{off-on},GT} + \alpha_{GB,t} C_{\text{off-on},GB} + \alpha_{\mathrm{coal},t} C_{\text{off-on,coal}} \right) \\
&C_E = \sum_{t=1}^{T} \left(\eta_{e,IL} P_{e,IL,t} + \eta_{h,IL} P_{h,IL,t} + \eta_{e,Y} P_{e,Y,t} + \eta_{h,Y} P_{h,Y,t} \right)
\end{aligned}
\tag{22}
$$

In this formulation, the objective is to minimize the IES operating cost. $C_{\mathrm{IES,BiRO}}$ signifies total IES cost over one scheduling period, considering uncertainty in wind, PV, electrical load, and thermal load; u signifies uncertain variables corresponding to wind, PV, electrical load, and thermal load. U is uncertainty set of the IES; C_A signifies IES energy purchase cost; $W_{\mathrm{gas,price},t}$ and $W_{\mathrm{electricity,price},t}$ signify system natural gas purchase price and electricity purchase price; $W_{\mathrm{coal,price}}$ signifies coal purchase price; C_B signifies penalty cost for curtailed wind and PV; $\eta_{ab,WT}$ and $\eta_{ab,PV}$ signify penalty coefficients for wind curtailment and PV curtailment; $P_{ab,WT,t}$ and $P_{ab,PV,t}$ signify wind curtailment and PV curtailment amount; C_C signifies operating costs of individual units in the IES; $P_{e,WT,t}$ and $P_{e,PV,t}$ signify electrical power outputs of WT and PV; β_{WT}, β_{PV}, β_{GT}, β_{GB} and β_{coal} signify operating cost coefficients for WT, PV, GT, GB and coal fired units. C_D signifies startup and shutdown cost vector for IES units; $\alpha_{GT,t}$, $\alpha_{GB,t}$ and $\alpha_{\mathrm{coal},t}$ signify operating state variables for GT, GB and coal fired units (1 indicates on, 0 indicates off); $C_{\text{off-on},GT}$, $C_{\text{off-on},GB}$ and $C_{\text{off-on,coal}}$ signifies single event startup and shutdown costs for GT, GB and coal fired units; C_E signifies IDR related cost for the system; $\eta_{e,IL}$, $\eta_{h,IL}$, $\eta_{e,Y}$, $\eta_{h,Y}$ signify economic compensation coefficients for interruptible electric and thermal loads and for shiftable electric and thermal loads. C_{CO2} represents the system's carbon emission cost, and C_{CT} represents the system's carbon trading cost.

3.3 Constraints

(1) Electrical balance constraint [37]

$$\hat{P}_t^{\mathrm{pv}} + \hat{P}_t^{\mathrm{wt}} + P_t^{\mathrm{buy}} + P_t^{\mathrm{GT}} + P_t^{\mathrm{g\_0}} + P_t^{\mathrm{bt,dis}} = P_t^{\mathrm{load}} + P_t^{\mathrm{P2A}} + P_t^{\mathrm{CCPP}} + P_t^{\mathrm{W}} \tag{23}$$

where $\hat{P}_t^{\mathrm{pv}}$ and $\hat{P}_t^{\mathrm{wt}}$ denote the forecasted wind and PV outputs; P_t^{g0} is the coal-fired unit generation; P_t^{CCPP} is the CCPP operating energy consumption; P_t^{W} is the curtailed renewable power; $P_t^{\mathrm{bt,dis}}$ is the hydrogen fuel cell discharge power; P_t^{load} is the electricaad.

(2) Thermal balance constraint

$$H_t^{\mathrm{HFC}} + H_t^{\mathrm{HB}} + H_t^{\mathrm{WHB}} + H_t^{\mathrm{P2A}} + P_t^{\mathrm{dist,dis}} = P_t^{\mathrm{tst,ch}} + H_t^{\mathrm{load}} \tag{24}$$

where H_t^{HFC} is the thermal power output of the hydrogen fuel cell; H_t^{WHB} is the thermal power output of the waste heat boiler; H_t^{HB} is the thermal power output of the gas boiler; H_t^{P2A} is the P2A waste heat recovery power; $P_t^{\mathrm{tst,ch}}$ and $P_t^{\mathrm{dist,dis}}$ are the thermal storage charge and discharge powers; H_t^{load} is the thermal load.

(3) Electrolyzer constraints

The reserve capacity deliverable by the electrolyzer is constrained by its energy consumption bounds and the hydrogen tank capacity, as expressed in Eq. (25):

$$\begin{cases} 0 \le R_t^{H_2,u} \le \min\left\{P_t^{H_2}, \frac{M_t^{\mathrm{hs}} H_{H_2}}{\eta^{H_2}\eta_{\mathrm{hs}}^{\mathrm{in}}}\right\} \\ 0 \le R_t^{H_2,d} \le \min\left\{P_{\max^{H_2}} - P_t^{H_2}, \frac{\left(M_{\max^{\mathrm{hs}}} - M_t^{\mathrm{hs}}\right) H_{H_2}}{\eta^{H_2}\eta_{\mathrm{hs}}^{\mathrm{in}}}\right\} \end{cases} \tag{25}$$

where $R_t^{H_2,u}$ and $R_t^{H_2,d}$ are the upward and downward reserve capacities provided by the electrolyzer; $P_{\max^{H_2}}$ and $M_{\max^{\mathrm{hs}}}$ denote the maximum energy consumption of the electrolyzer and the maximum capacity of the hydrogen storage tank.

$$\begin{cases} 0 \le M_t^{\mathrm{bs}} \le M_{\max}^{\mathrm{bs}} \\ M_0^{\mathrm{bs}} = M_{24}^{\mathrm{bs}} = 0.5 M_{\max}^{\mathrm{bs}} \end{cases} \tag{26}$$

where M_0^{bs} and M_{24}^{bs} denote the hydrogen mass in the storage tank at the initial and final time points of the scheduling horizon.

(4) GB constraints

The GB thermal output is subject to lower and upper bounds.

$$\alpha_{GB,t} P_{h,GB,\min} \le P_{h,GB,t} \le \alpha_{GB,t} P_{h,GB,\max} \tag{27}$$

where $P_{h,GB,\max}$ and $P_{h,GB,\min}$ are the lower and upper bounds of GB thermal output.

(5) GT constraints

Considering the GT as a controllable generator, its operation is constrained by power output bounds and ramping limits.

$$\begin{cases} \alpha_{GT,t} P_{e,GT,\min} \le P_{e,GT,t} \le \alpha_{GT,t} P_{e,GT,\max} \\ R_{down,GT} P_{e,GT,\max} \le P_{e,GT,t} - P_{e,GT,t-1} \le R_{lp,GT} P_{e,GT,\max} \end{cases} \tag{28}$$

where $P_{e,GT,\max}$ and $P_{e,GT,\min}$ are the lower and upper bounds of GT electrical output, $R_{lp,GT}$ and $R_{down,GT}$ denote the GT ramp-up and ramp-down limits within a scheduling interval.

(6) WHB operation constraints

The WHB recovery of GT waste heat and the WHB thermal output are subject to thermal power bounds [38].

$$\alpha_{WHB,t}P_{h,WHB,\min} \le P_{h,WHB,t} \le \alpha_{WHB,t}P_{h,WHB,\max} \tag{29}$$

where $\alpha_{WHB,t}$ is the WHB operation state variable (1 denotes on, 0 denotes off).

(7) HFC constraints [39]

Like the electrolyzer, the HFC operation is subject to power magnitude, ramping range, and fuel cell stack temperature constraints.

$$\begin{cases} \zeta_{\mathrm{hfc},\min}\delta_{\mathrm{hfc},t}C_{\mathrm{ap,hfc}} \le P_{\mathrm{hfc,in},t} \le \zeta_{\mathrm{hfc},\max}\delta_{\mathrm{hfc},t}C_{\mathrm{ap,hfc}} \\ \left|P_{\mathrm{hfc,in},t} - P_{\mathrm{hfc,in},t-1}\right| \le \Delta P_{\mathrm{hfc},\max} \\ T_{\mathrm{hfc},\min} \le T_{\mathrm{hfc},t} \le T_{\mathrm{hfc},\max} \end{cases} \tag{30}$$

where $\zeta_{\mathrm{hfc},\max}$ and $\zeta_{\mathrm{hfc},\min}$ denote the fuel cell maximum and minimum load factors; $\delta_{\mathrm{hfc},t}$ is a 0 1 variable indicating whether the fuel cell is operating at the current time; $C_{\mathrm{ap,hfc}}$ is the installed capacity of the fuel cell; $\Delta P_{\mathrm{hfc},\max}$ is the maximum ramp power of the fuel cell per time period; $T_{\mathrm{hfc},\max}$ and $T_{\mathrm{hfc},\min}$ are the lower and upper bounds of the fuel cell stack operating temperature.

(8) Power consumption constraints for ASU and ammonia synthesis

$$P_{s,t}^{\mathrm{NS}} = \phi n_{s,t}^{\mathrm{N_2}} = \frac{1}{3}\phi n_{s,t}^{\mathrm{H_2,out}}, \forall s \in \Omega, t \in T \tag{31}$$

$$P_{s,t}^{\mathrm{AS}} = \psi n_{s,t}^{\cdot\mathrm{NH_3}} = \frac{2}{3}\psi n_{s,t}^{\cdot\mathrm{H_2,out}}, \forall s \in \Omega, t \in T \tag{32}$$

where ϕ and ψ are the energy consumption coefficients for the air separation unit and the ammonia synthesis process in the P2A system.

(9) Ammonia production upper and lower bound constraints

$$\mu_{s,l}^{\mathrm{AS}}K^{\mathrm{AS},\min}\hat{n}_{s,l}^{\mathrm{NH_3}} \le \hat{n}_{s,l}^{\mathrm{H_2,out}} \le \mu_{s,l}^{\mathrm{AS}}K^{\mathrm{AS},\max}\hat{n}_{s,l}^{\mathrm{NH_3}}, \forall s \in \Omega, t \in T \tag{33}$$

where μ_t^{AS} is the startup variable of the P2A reactor, $K^{\mathrm{AS},\max}$ and $K^{\mathrm{AS},\min}$ are the lower and upper bounds of hydrogen flow into the ammonia reactor.

(10) Ammonia blending ratio constraint

Because ammonia cofiring affects furnace combustion characteristics, the ammonia blending ratio is limited as [40]:

$$0 \le y_1 \le y_{\max} \tag{34}$$

where $y_{\max}$ denotes the allowable maximum ammonia blending ratio. In this study, the upper limit of the blending ratio is set to 20%.

(11) Coal-fired unit ramping constraints

$$\begin{cases} -\Delta P_{\max^{\mathrm{th,th}}} \le P_t^{\mathrm{th,th}} - P_{t-1}^{\mathrm{th,th}} \le \Delta P_{\max^{\mathrm{th,th}}} \\ -\Delta P_{\max^{\mathrm{th,chp}}} \le P_t^{\mathrm{th,chp}} - P_{t-1}^{\mathrm{th,chp}} \le \Delta P_{\max^{\mathrm{th,chp}}} \\ -\Delta H_{\max^{\mathrm{th,chp}}} \le H_t^{\mathrm{th,chp}} - H_{t-1}^{\mathrm{th,chp}} \le \Delta H_{\max^{\mathrm{th,chp}}} \end{cases} \tag{35}$$

where $\Delta P_{\max^{\text{th,th}}}$ is the maximum allowable ramp power for a coal-fired generation unit. $\Delta P_{\max^{\text{th,chp}}}$ and $\Delta H_{\max^{\text{th,chp}}}$ are the maximum allowable ramp powers for electrical output and thermal output of a cogeneration unit.

(12) P2A equipment ramping constraints

The P2A plant's ramp-up and ramp-down ceilings are set at 10% and 20% of nameplate capacity, respectively, and production rate may be altered no more than once within any four-hour window.

$$\begin{cases} -20\%P_{\max^{\text{P2A}}} \le P_t^{\text{P2A}} - P_{t-1}^{\text{P2A}} \le 10\%P_{\max^{\text{P2A}}} \\ P_{t+1}^{\text{P2A}} = P_t^{\text{P2A}}, \quad t \in [4i+1, 4i+3], \quad i \in \{0 \sim 5\} \end{cases} \tag{36}$$

(13) Power purchase and sale bounds

$$P_{\min}^{\text{grid}} \le P_{s,t}^{\text{RE2A,grid}} \le P_{\max}^{\text{grid}}, \forall s \in \Omega, t \in T \tag{37}$$

(14) CCPP equipment constraints

$$\begin{cases} P_t^{\text{CCPP}} = \gamma_{\text{e}} Q_t^{\text{c}} \\ Q_t^{\text{c}} = \eta_t \left(\epsilon_{\text{MT}} P_t^{\text{MT}} + \epsilon_{\text{GB}} H_t^{\text{GB}} \right) \end{cases} \tag{38}$$

where γ_{e} is the electric power consumed per unit CO_2 captured; η_t is the carbon capture rate of CCPP; Q_t^{c} is the amount of CO_2 captured by the CCPP; ϵ_{MT} and ϵ_{GB} are the carbon emission coefficients of the gas turbine and the gas boiler.

(15) Ammonia storage tank constraints

The mass balance and charging discharging limits of the ammonia tank are as follows:

$$\begin{cases} m_t^{\text{as}} = m_{t-1}^{\text{as}} + m_t^{\text{as+}} - m_t^{\text{as-}} \\ m_1^{\text{as}} \le m_t^{\text{as}} \le m_u^{\text{as}} \\ m_1^{\text{as+}} \le m_t^{\text{as+}} \le m_u^{\text{as+}} \\ m_1^{\text{as-}} \le m_t^{\text{as-}} \le m_u^{\text{as-}} \end{cases} \tag{39}$$

where m_t^{as}, $m_t^{\text{as+}}$ and $m_t^{\text{as-}}$ denote the stored ammonia mass, the ammonia charging amount, and the ammonia discharging amount; m_1^{as} and m_u^{as}, $m_1^{\text{as+}}$ and $m_u^{\text{as+}}$, $m_1^{\text{as-}}$ and $m_u^{\text{as-}}$ denote the lower and upper bounds for storage, charging, and discharging quantities. The ammonia exported from the storage tank, denoted $m_t^{\text{as-}}$, is the hourly ammonia demand for sale and is treated as a fixed value in this study.

(16) Thermal storage tank operation constraints

The TSK is subject to capacity bounds and charge discharge power limits [23].

$$\begin{cases} Q_{HST,\min} \le Q_{HST,t} \le Q_{HST,\max} \\ 0 \le P_{h,HST,ch,t} \le P_{h,HST,ch,\max} \\ 0 \le P_{h,HST,\text{dis},t} \le P_{h,HST,\text{dis},\max} \\ P_{h,HST,ch,t} \cdot P_{h,HST,\text{dis},t} = 0 \end{cases} \tag{40}$$

where $Q_{HST,\max}$ and $Q_{HST,\min}$ denote the lower and upper bounds of thermal storage tank storage capacity; $P_{h,HST,ch,\max}$ and $_{h,HST,\text{dis},\max}$ denote the maximum charging power and maximum discharging power of the thermal storage tank.

3.4 Solution Method

The above two-stage robust optimization model is solved using the column-and-constraint generation (C&CG) algorithm. The detailed solution procedure is provided in the Fig. 8.

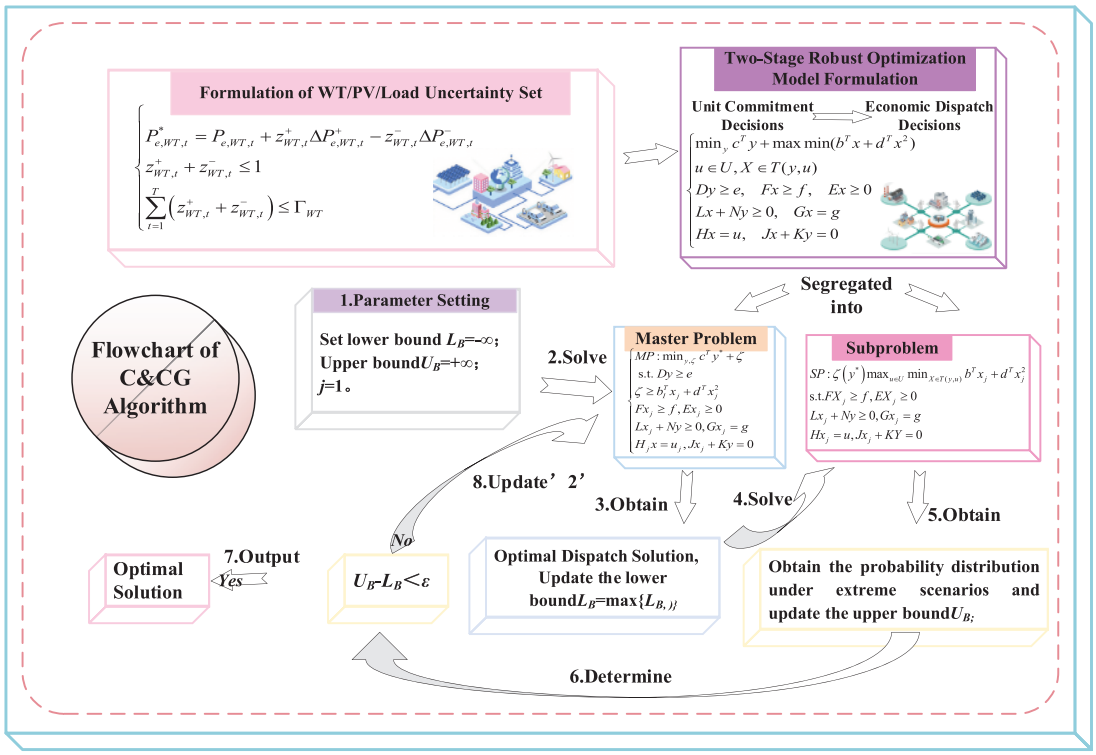

Figure 8: Flowchart of two-stage robust dispatch

4 Case Study

The case study is implemented on the MATLAB R2022a platform. Problem instances are formulated in YALMIP and solved using the IBM ILOG CPLEX solver.

4.1 Parameter Settings

To validate the proposed model in terms of scheduling performance, energy saving, emission reduction, and robustness against stochastic fluctuations, a representative IES depicted in Fig. 1 is selected for numerical analysis. Major components include a P2A facility, coal-fired generation units, wind and PV, carbon capture, and hydrogen utilization units. Relevant parameters are listed in Table 1. Time-varying electricity and natural gas prices are given in Fig. 9a, and the forecast profiles for renewable generation and loads are shown in Fig. 9b. Latin hypercube sampling is used to generate 1000 samples, which K-means cluster into 10 representative scenarios for wind, PV, and load; the typical scenario generation results are presented in Appendix A, Fig. A1.

Table 1: Main parameters used in the model

Stepped carbon trading mechanism	Base carbon price (CNY/t)	200
	Increase rate	25%
	Actual step prices (CNY/kg)	[0.2, 0.25, 0.3]
Ammonia fuel properties	Ammonia density (kg/m^3)	0.771
	Ammonia mass calorific value (kWh/kg)	5.82
	Ammonia volumetric calorific value (kWh/m^3)	4.49
Other fuel calorific values	Coal calorific value (kWh/kg)	8.14
	Gas boiler natural gas calorific value (kWh/m^3)	9
	Gas turbine natural gas calorific value (kWh/m^3)	7.5
Cost compensation coefficients	Electrical/Heat load shift compensation (CNY/kWh)	0.26/0.5
	Electrical/Heat load interruption compensation (CNY/kWh)	0.7/0.9
	Wind/PV curtailment penalty coefficient (CNY/kWh)	1
	Thermal power operating cost coefficient (CNY/kWh)	0.03
	Thermal unit startup/shutdown cost (CNY/cycle)	1.6
	Ammonia cofiring revenue coefficient (CNY/kWh)	0.0947
Equipment capacity limits	Thermal power unit output (MW)	120, 400
	Gas turbine output (MW)	50, 200
	Fuel cell (MW)	0, 300
	Electrolyzer (MW)	0, 300
	Grid purchase limit (MW)	160
	PSA unit (MW)	0, 200
	Gas boiler (MW)	0, 300
	P2A ammonia production unit (MW)	0, 100
	Waste heat boiler (MW)	0, 100
	Hydrogen storage tank (Volume, m^3)	600,000
	Ammonia storage tank (Volume, m^3)	400,000
	Thermal storage tank (Energy Capacity, kWh)	240,000
Energy conversion efficiency	Alkaline electrolyzer (Electricity to Hydrogen)	67%
	Fuel cell (Hydrogen to Electricity)	85%
	Gas turbine power generation efficiency (Gas to Electricity)	35%
	Gas turbine cogeneration efficiency	40%
	Gas boiler efficiency (Gas to Heat)	70%
Energy storage charge/discharge efficiency	Hydrogen storage	90%
	Ammonia storage	95%
	Thermal storage	90%

(Continued)

Table 1 (continued)

Ramp rate constraints	Thermal power unit (MW/h)	±100
	Gas turbine (MW/h)	±150
	Gas boiler (MW/h)	±25
Demand response ratio constraints	Electrical load shift ratio	±15%
	Electrical load curtailment ratio	10%
	Heat load shift ratio	±15%
	Heat load curtailment ratio	10%
Waste heat recovery system	Waste heat boiler power-to-heat ratio	1.47
	Waste heat boiler heat recovery efficiency	80%
	Ammonia waste heat recovery coefficient (MW heat/MW ammonia)	0.1187
Carbon emission coefficients	Thermal power unit (t-CO_2/MWh)	0.9
	Gas turbine (t-CO_2/MWh)	0.4
	Gas boiler (t-CO_2/MWh)	0.4
Carbon capture system	Specific capture energy consumption (kWh/t-CO_2)	370
	Carbon allowance benchmark for thermal power (t-CO_2/MWh)	0.7
	Carbon allowance benchmark for gas-fired units (t-CO_2/MWh)	0.15
Ammonia cofiring parameters	Maximum ammonia cofiring ratio	20%
	Ammonia cofiring cost coefficient (CNY/kWh)	−0.0947

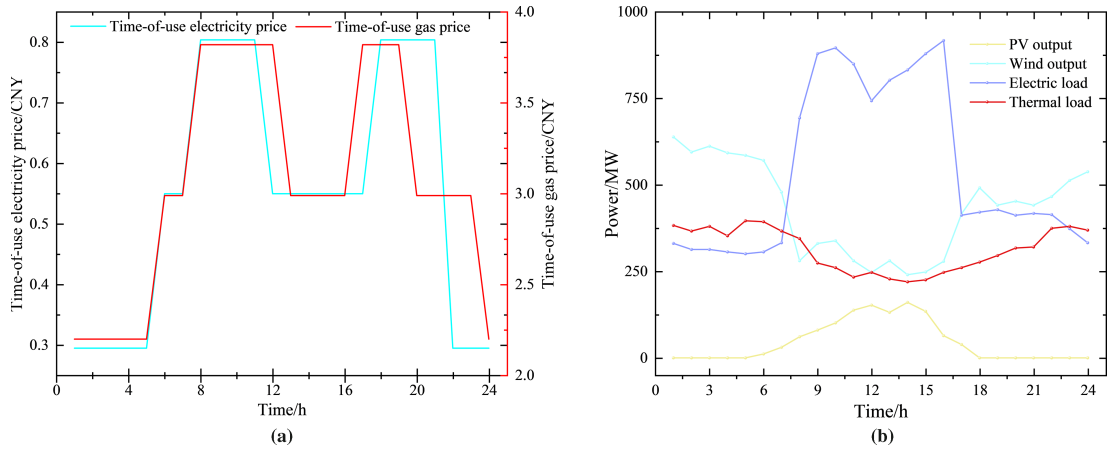

Figure 9: Time of use, electricity and gas prices, and forecast profiles for wind and PV. (**a**) Time of use electricity and gas prices; (**b**) Forecast profiles for WT, PV, and loads

4.2 Uncertainty Sets

The 10 representative wind and PV scenarios obtained by clustering are directly embedded into the optimization model as mandatory operating conditions, forcing the dispatch plan to adapt to their fluctuation characteristics. Simultaneously, for load and PV forecast errors, robust optimization constructs uncertainty intervals for load and renewable fluctuations and uses budget parameters to control the frequency of worst-case occurrences.

The load uncertainty budget parameter is set to 12, and the PV uncertainty budget parameter to 6. This means that during dispatch optimization, load power may take the maximum of its forecast interval in at most 12 time periods, and PV output may take the minimum of its forecast interval in at most 6 time periods; in other periods, the values equal the forecasts. In practice, allowable maximum forecast deviations for microgrid load and PV output can be set based on historical forecast error statistics. In this study, the forecast deviation margins are 10% for load power and 15% for PV output. Fig. 10a–d shows the forecast and worst-case load and PV curves, where shaded areas represent the uncertainty sets considered.

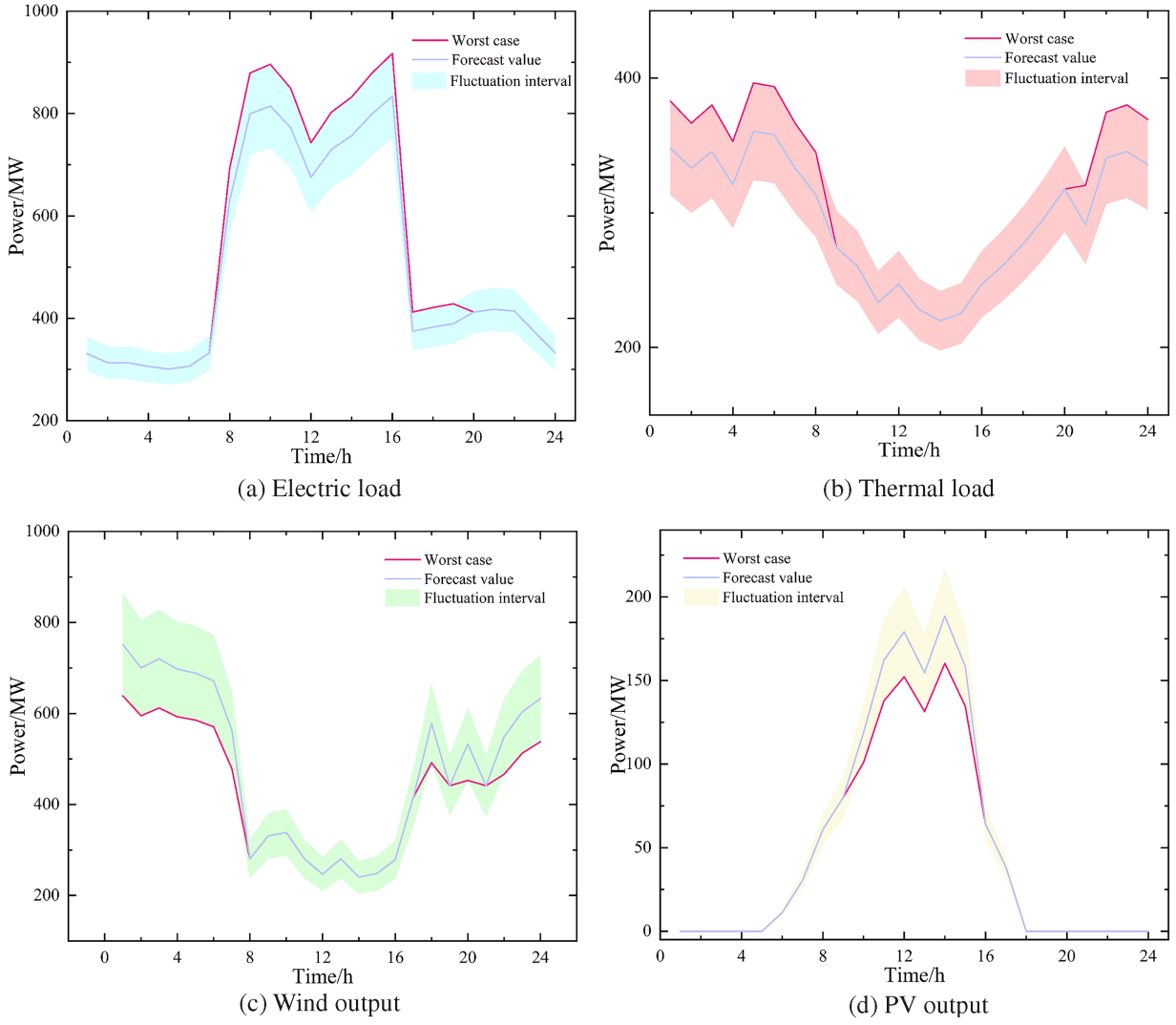

Figure 10: Illustration of uncertainty sets

4.3 Design of Scenarios

To comprehensively assess the effectiveness of the IES dispatch model that considers ammonia cofiring and DR, four optimization scenarios are defined:

Scenario 1: Baseline hydrogen scheduling model (Including wind and PV-driven hydrogen production, hydrogen fuel cells, stepwise carbon trading, scenario generation method, two-stage robust optimization);

Scenario 2: Scenario 1 plus curtailment-driven CCPP;

Scenario 3: Scenario 2 augmented with ammonia utilization;

Scenario 4: Scenario 3 plus electric and thermal IDR.

4.4 Analysis of Dispatch Results for Each Scenario

Table 2 summarizes key dispatch results of the IES under the four operating scenarios.

Table 2: Dispatch results under different operating scenarios

Scenario	1	2	3	4
Operating cost/10,000CNY	718.54	638.93	615.34	451.07
Coal cost/10,000CNY	55.7	55.6	50.54	46.452
Electricity purchase cost/10,000CNY	5.74	8.71	5.42	0
Gas purchase cost/10,000CNY	286.97	287.12	268.01	260.5
Carbon trading cost/10,000CNY	60.766	32.787	27.535	19.63
Carbon emissions/t	2870.84	1490.66	1452.41	917.6
Renewable curtailment rate/%	24.05%	20.69%	15.62%	3.17%
CCS energy consumption/MW	0	373.02	373.02	382.43
Total ammonia cofiring/MW	0	0	332.53	870.40
IDR cost/10,000CNY	0	0	0	11.25

Scenario 1 employs the baseline hydrogen utilization dispatch strategy and does not include carbon capture. Under this scenario, renewable curtailment and carbon emissions are relatively high. The system requires substantial natural gas purchases to meet demand, resulting in peak operating costs and carbon emissions.

Scenario 2 introduces the curtailment-driven carbon capture plant (CCPP) to Scenario 1. The CCPP operates flexibly, consuming only surplus renewable energy that would otherwise be curtailed. Despite its reduced annual operation, this strategy creates outsized system value. It eliminates the primary energy cost of carbon capture and leverages the stepwise carbon price. The results confirm its efficacy: renewable curtailment decreases by 4.5%, and a massive emission reduction of 1380 t (47%) slashes carbon trading costs

by CNY 279,800. The total operating cost falls by 11.12%. This demonstrates that the synergistic benefits of avoided carbon penalties and zero-cost energy can economically justify the flexible operation of the CCPP, validating it as a key system asset for simultaneous economic and environmental improvement.

Scenario 3 further introduces P2A and waste heat recovery based on Scenario 2 and implements ammonia cofiring. The P2A facility absorbs 466 mw of curtailed wind and PV power and produces 332.5 mw of ammonia energy, realizing chemical storage of renewable energy. The produced green ammonia replaces coal and reduces unit fuel cost by CNY 51,000 (a 9.11% reduction); recovery of synthesis waste heat lowers gas heating consumption, and thus gas purchase cost decreases by 6.62%. System operating cost and carbon emissions decrease further relative to Scenario 2 by 7.95% and 11.41%, respectively. This scenario significantly enhances the IES performance regarding low-carbon operation and economic efficiency through reduced coal consumption and emissions. Furthermore, the waste heat recovered from the P2A process in Scenario 3 amounted to 166 mw of thermal energy. This contributed to approximately 2.2% of the system's total daily thermal load, quantitatively demonstrating the role of ammonia synthesis in supporting the heat supply and enhancing overall energy utilization.

Scenario 4 builds on Scenario 3 by introducing IDR. Time of use electricity and gas price signals dynamically guide load adjustments, enabling deep coordination between demand side resources and the ammonia energy system, and forming a dynamic optimization closed loop of "supply following load and ammonia smoothing peaks and filling valleys". IDR shifts 12.7% of peak period electric load to periods of high renewable output, creating sustained green power windows for P2A. Ammonia cofiring increases from 332.5 to 870.4 mw. This indirectly helps coal-fired unit fuel cost decline by 8.1%, and system carbon emissions fall by 36.8%. Temporal and spatial shifting of electric and thermal loads reduces gas peaking pressure, lowering gas purchase cost by 2.8%. An IDR investment of CNY 112,500 leverages a total system cost reduction of CNY 1,642,700; the renewable curtailment rate falls to 3.17%. This scenario successfully unlocks the zero-carbon closed-loop potential of green ammonia, achieving combined benefits of reduced fuel cost and lower emissions.

Electric and thermal power balance plots for the four scenarios are given in Figs. 11–14.

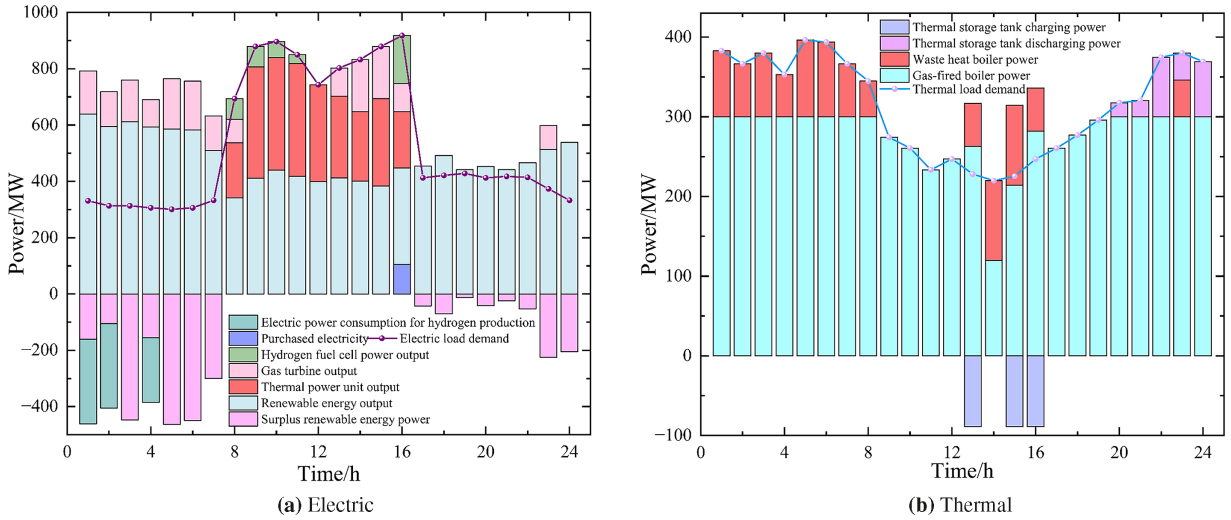

(a) Electric **(b)** Thermal

Figure 11: Scenario 1 power balance

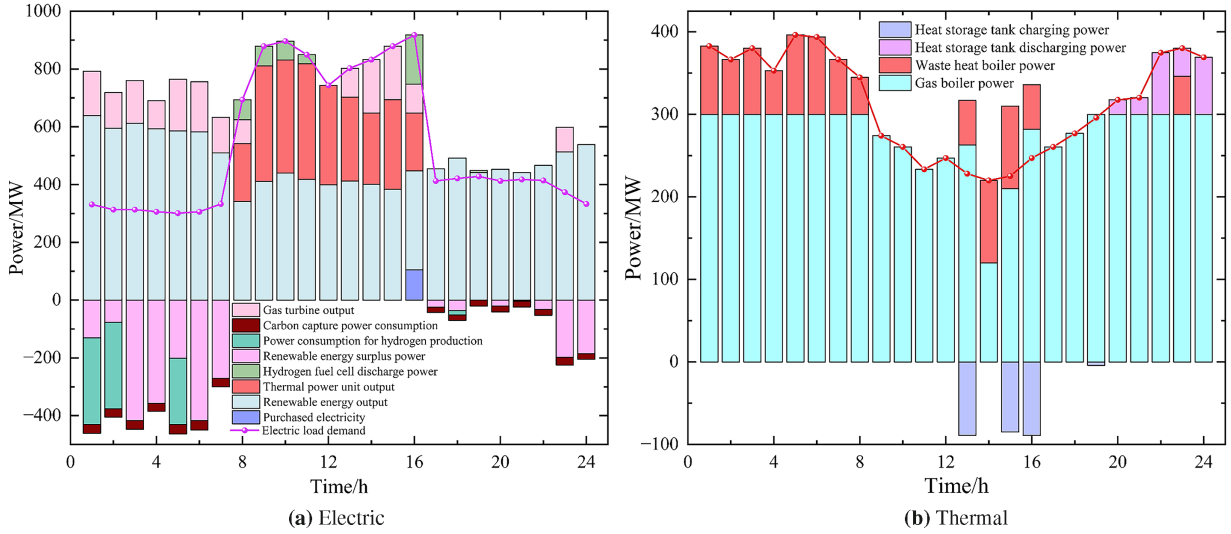

(a) Electric **(b)** Thermal

Figure 12: Scenario 2 power balance

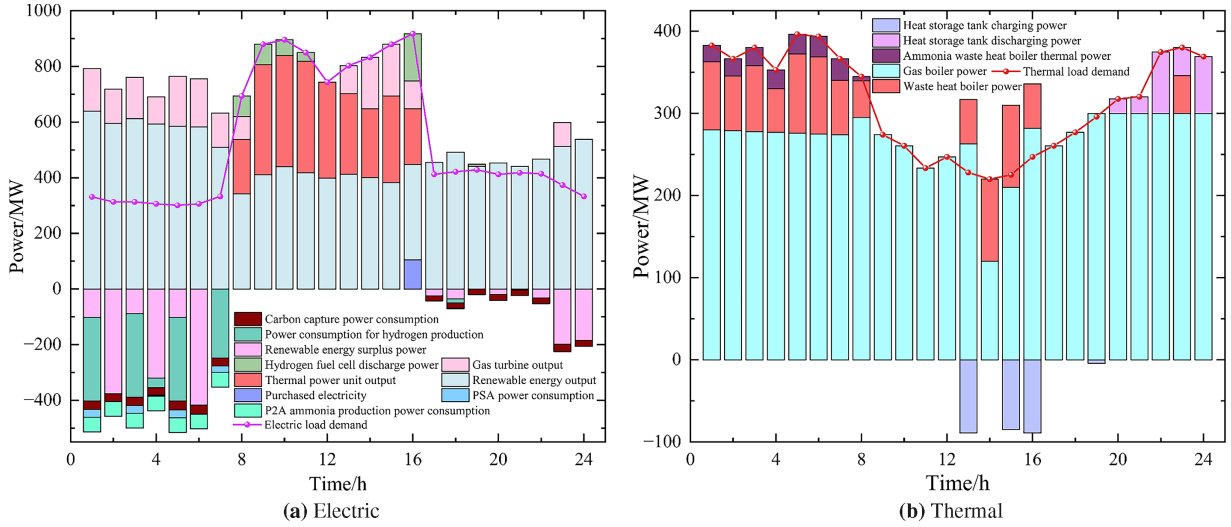

(a) Electric **(b)** Thermal

Figure 13: Scenario 3 power balance

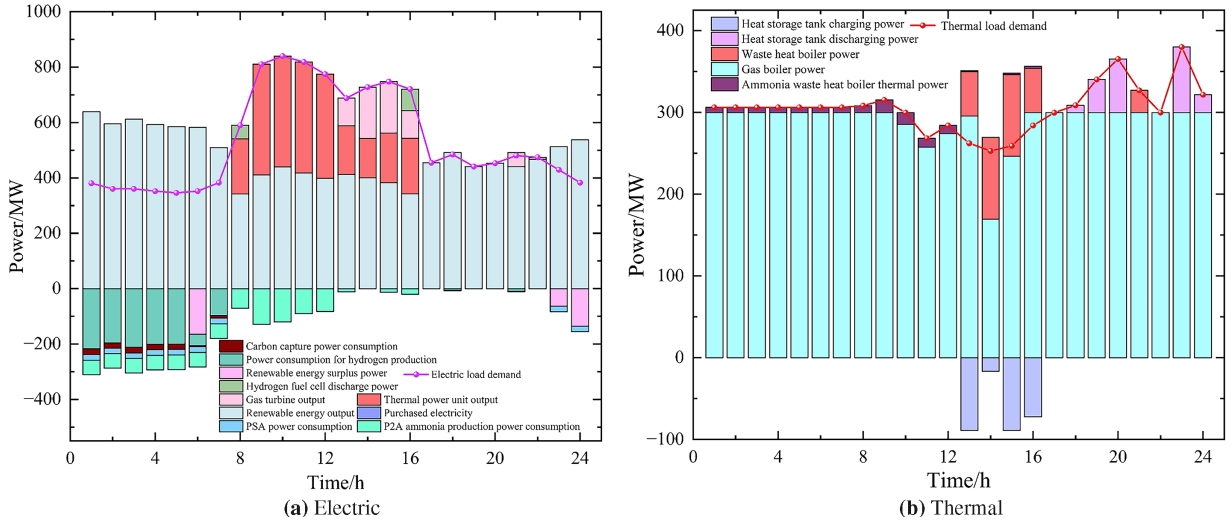

(a) Electric **(b)** Thermal

Figure 14: Scenario 4 power balance

4.5 Carbon Emission and Capture Analysis

Fig. 15a,b presents the dynamic changes in carbon emissions and capture following the integration of carbon capture plants. Analysis of Scenario 1's power balance reveals that during 00:00–05:00 and 16:00–24:00, surplus renewable output is available, which is directed to the carbon capture system to reduce CO_2 emissions actively. The total CO_2 emissions decrease from 2.872 t in the base case to 1.491 t, representing a 48.08% reduction, confirming the effectiveness of coordinated renewable utilization and carbon capture in emission reduction.

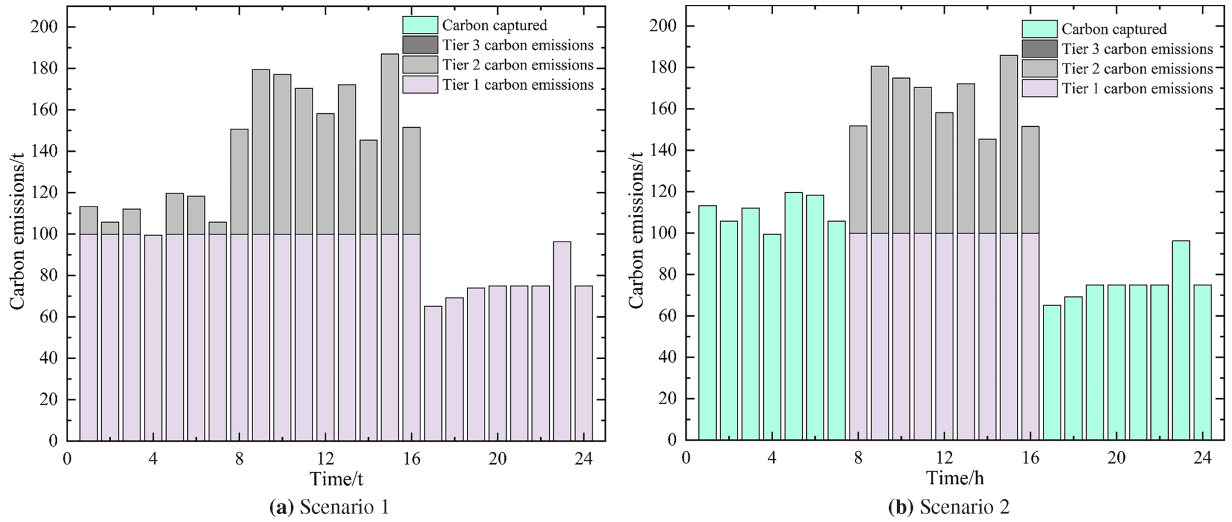

(a) Scenario 1 **(b)** Scenario 2

Figure 15: Carbon emission and capture analysis

Fig. 16 compares renewable energy curtailment before and after introducing carbon capture driven by surplus energy, showing a clear improvement in wind-PV utilization.

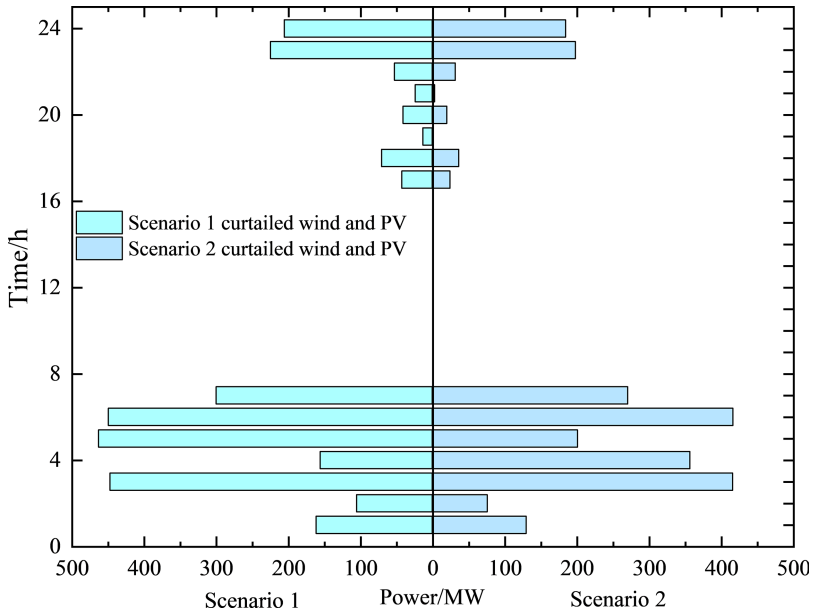

Figure 16: Comparison of curtailed energy utilization in CCPP

4.6 Power-to-Ammonia Utilization Analysis

The ammonia energy utilization in Scenario 3 is shown in Fig. 17. Fig. 17a shows that P2A ammonia production mainly occurs during 01:00–07:00 when renewable output exceeds demand. Ammonia is stored in tanks, with no ammonia cofiring in coal units. Between 08:00–14:00, when load demand peaks and renewable output is insufficient, coal units operate with ammonia cofiring, drawing on stored ammonia. Some ammonia remains stored to buffer against future demand fluctuations or extreme events.

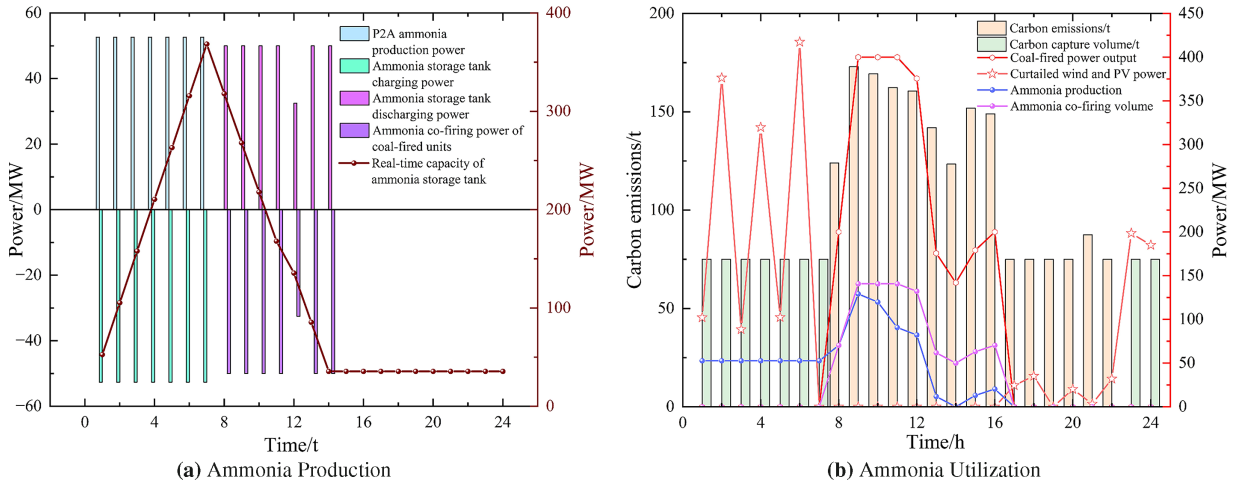

Figure 17: Ammonia utilization analysis

Fig. 17b shows that when ammonia production spikes between 07:00–09:00, ammonia cofiring output also increases sharply. Coal unit output even rises significantly (from 0 to 400 mw) between 09:00–11:00 due to the substitution of green ammonia for coal, reducing coal consumption while maintaining generation capacity. Between 00:00–07:00, renewable output fluctuates sharply, with P2A operating at a

low, stable level. From 08:00 onward, renewable output exceeds the baseline grid absorption capacity, prompting a rapid ramp-up of ammonia production and continuous operation until 16:00, resulting in full renewable utilization.

4.7 Ammonia Cofiring Ratio Analysis

As shown in Fig. 18a,b, increasing the cofiring ratio from 0% to 20% continuously reduces operating costs from 4.7924 to 4.3507 million CNY, although marginal benefits diminish. In the 0%–6% range, cost reduction reaches 375,200 CNY, whereas in the 6%–20% range, it is only 66,500 CNY.

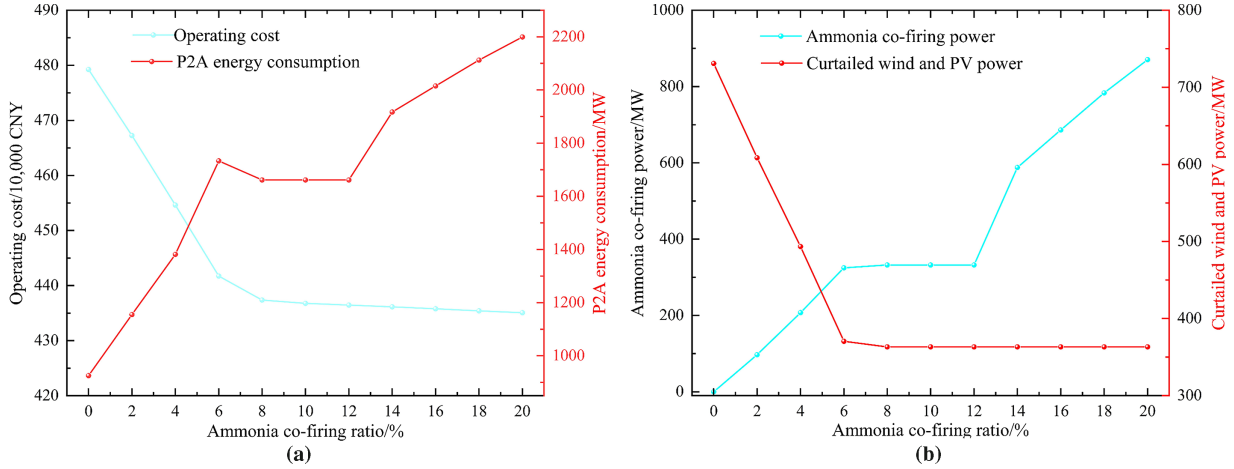

Figure 18: Ammonia cofiring ratio analysis. (**a**) Operating cost and P2A energy consumption; (**b**) Cofiring power and curtailment

Renewable energy absorption saturates at a 6% cofiring ratio, with wind-PV curtailment dropping from 730.9 to 370.44 mw and stabilizing around 363.21 mw, indicating that 6% represents the maximum curtailment reduction potential under current grid and P2A constraints.

4.8 DR Effect Analysis

Fig. 19a,b shows that after the introduction of IDR, deep coordination between demand side resources and the ammonia energy system is achieved. As illustrated in Figs. 14 and 19a,b, IDR shifts shiftable electric load in the 08:00–16:00 window under electricity price signals to periods of high wind and PV output, effectively reducing grid electric load during that interval. Simultaneously, parts of the shiftable thermal load from other periods are shifted into the 08:00–16:00 window, producing coordinated temporal optimization of electric and thermal loads.

This operation substantially frees up grid capacity during 08:00–16:00, enabling surplus renewable electricity to be efficiently allocated to P2A production and driving a substantial increase in green ammonia output. At the same time, the temporal redistribution of thermal load combined with P2A waste heat recovery improves heat supply and demand matching and alleviates peaking pressure on gas turbine units.

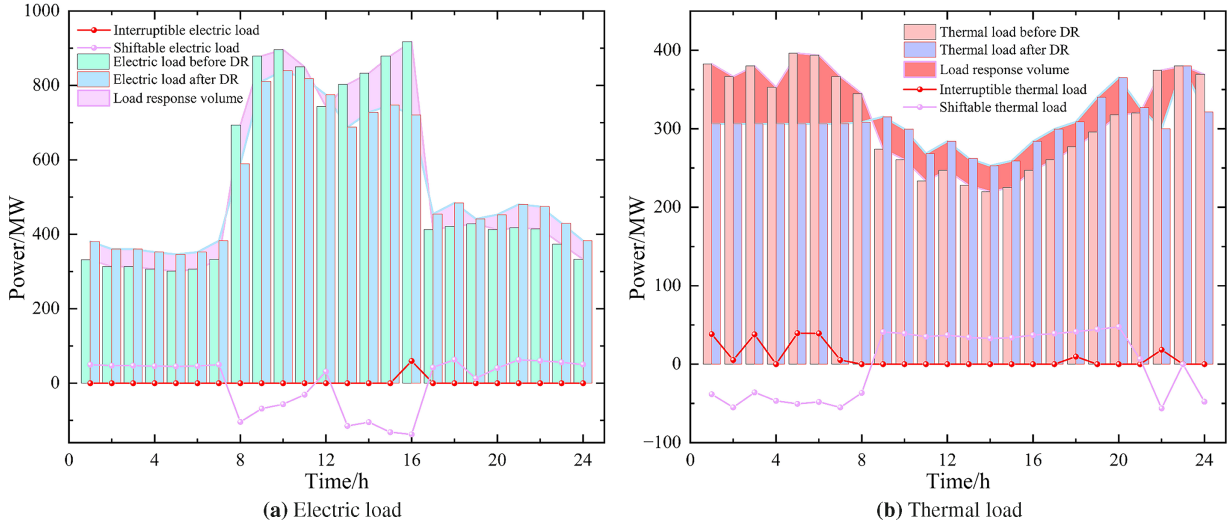

(a) Electric load **(b)** Thermal load

Figure 19: Comparison of electric and thermal load before and after DR

4.9 Impact of Carbon Price Base Level

Fig. 20a,b reports the system response under a stepwise carbon price policy simulated over CNY 0–0.5 per ton range. In the low price range CNY 0–0.1 per ton, the system maintains a high emission level of approximately 1880 t; limited ammonia cofiring yields only marginal emission reductions while user satisfaction remains about 98.6%. When the carbon price rises into the transition band CNY 0.15–0.25 per ton, carbon emissions decline markedly, and the ammonia cofiring power increases to around 870 mw, indicating activation of deeper decarbonization measures. Once the carbon price exceeds a threshold of CNY 0.3 per ton, the system enters a transformed steady state: ammonia co firing stabilizes near 860 mw and, together with coordinated CCPP operation, achieves net zero carbon emissions; however, operating cost stabilizes at approximately CNY 4.43 million and user satisfaction decreases to 97.5% due to reduced GB heat supply and increased proportion of thermal load interruptions. The analysis indicates that the carbon price band CNY 0.15–0.25 per ton yields the best cost effectiveness, whereas prices ≥ CNY 0.3 per ton drive a zero carbon transition at significantly higher system cost.

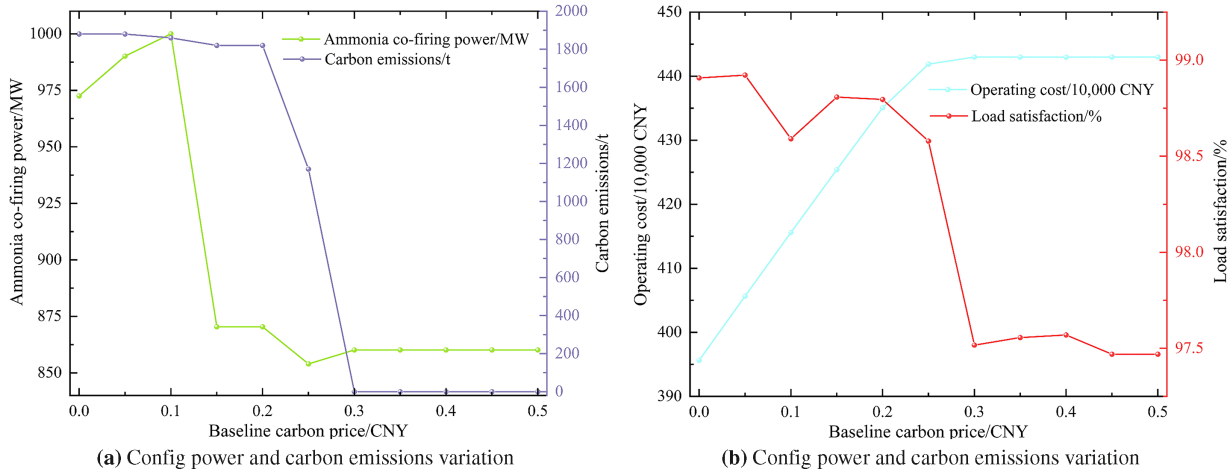

(a) Config power and carbon emissions variation **(b)** Config power and carbon emissions variation

Figure 20: Impact of base carbon price on system performance

5 Conclusions

This paper develops a two-stage robust optimization scheduling model for an IES incorporating P2A waste heat recovery and ammonia cofiring substitution. To address uncertainty, scenario generation and clustering are combined with a two-stage distributionally robust optimization framework. Case study results support the following conclusions:

(1) A curtailment-driven CCPP that consumes otherwise curtailed wind and PV power substantially enhances the system's carbon neutrality and energy utilization. After introducing the CCPP, renewable curtailment declines by 4.5%, total CO_2 emissions decrease by 1380 t (47% reduction), carbon trading cost declines by approximately CNY 279,800, and total operating cost falls by 11.12%, demonstrating clear synergistic benefits for both economics and environmental performance.

(2) The P2A facility converts curtailed wind and PV electricity into green ammonia and, combined with ammonia cofiring and waste heat recovery, absorbs 466 mw of curtailed renewable power and yields 332.5 mw equivalent ammonia energy. Green ammonia substituting coal reduces coal unit fuel cost by about CNY 51,000 and lowers gas heating demand and gas purchase cost by 6.62% via synthesis waste heat recovery. The system's total operating cost is reduced by 7.95% and CO_2 emissions decrease by 11.41%, yielding a substantive improvement in the system's low-carbon economic indicators.

(3) IDR enables the system to follow renewable availability and creates sustained green power windows for P2A. With IDR, the ammonia cofiring power increases from 332.5 to 870.4 mw, yielding an additional reduction of coal unit fuel cost by 8.1%. Temporal and spatial shifting of electric and thermal loads combined with waste heat recovery relieve gas peaking pressure and reduce gas purchase cost by 2.8%. An IDR investment of CNY 112,500 leverages a total system cost reduction of 26.7% and reduces renewable curtailment to 3.17%, effectively unlocking the low-carbon potential of green ammonia.

(4) The scenario generation and robust optimization coordinated framework effectively preserves the spatiotemporal correlation features of wind PV and load while dramatically reducing computational burden compared with naive high-dimensional formulations. The proposed approach improves system resilience: total system cost decreases by 37.2% and carbon emissions decline by 68.05% relative to the baseline, enabling the IES to maintain low cost, low emissions, and low curtailment even under extreme renewable output conditions.

While a future energy system may ideally rely solely on pure ammonia power generation, the approach of ammonia cofiring in existing coal-fired units presented in this study is positioned as a pragmatic transition strategy. It addresses the current reality of coal-dependent energy infrastructures by offering a feasible, low-retrofit, and cost-effective pathway for rapid decarbonization, bridging the gap between the present system and a future renewable-ammonia-based paradigm.

Acknowledgement: We extend our gratitude to the other authors for their contributions to this paper and their suggestions and efforts dedicated to this work.

Funding Statement: The authors received no specific funding for this study.

Author Contributions: The authors confirm contribution to the paper: Writing—original draft and conceptualization, Xingzuo Pan; data curation, Yi Ding; formal analysis, Zhilong Wei; methodology, Tonglin Liu; investigation, Jianxin Ni, Yupeng He; Writing—review& editing, Yupeng He. All authors reviewed the results and approved the final version of the manuscript.

Availability of Data and Materials: The data supporting this study's findings are available from the corresponding author, [Yupeng He], upon reasonable request.

Ethics Approval: Not applicable.

Conflicts of Interest: The authors declare no conflicts of interest to report regarding the present study.

Appendix A

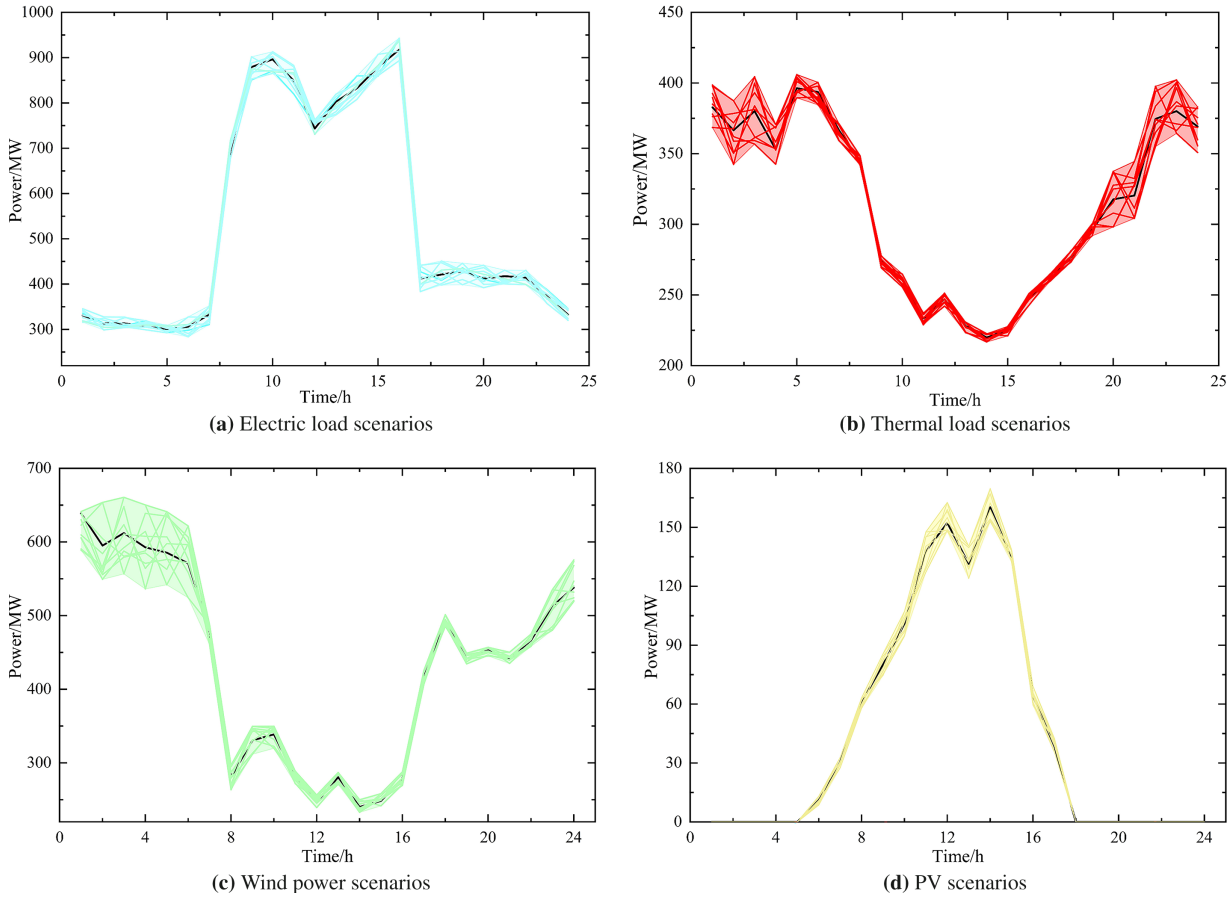

Figure A1: Typical scenarios generated for wind and load via clustering

References

1. Egeland-Eriksen T, Hajizadeh A, Sartori S. Hydrogen-based systems for integration of renewable energy in power systems: achievements and perspectives. Int J Hydrogen Energy. 2021;46(63):31963–83. doi:10.1016/j.ijhydene.2021.06.218.
2. Gupta V.R. S, Matapurkar P, Gupta P, Vikram R. Integration of solar and wind energy: a review of challenges and benefits. J Emerg Technol Innov Res. 2023;10(3):e604–9.
3. Tharun V, Kumar PS. A comprehensive review on hydrogen production, purification, storage, and utilization: challenges and future directions. Renew Sustain Energ Rev. 2025;224:116067. doi:10.1016/j.rser.2025.116067.
4. Zheng JH, Guo JC, Li Z, Wu QH, Zhou XX. Optimal design for a multi-level energy exploitation unit based on hydrogen storage combining methane reactor and carbon capture, utilization and storage. J Energy Storage. 2023;62:106929. doi:10.1016/j.est.2023.106929.

5. Sun Y, Li Z, Wang Q, Zhang J, Kong H. Low carbon pathway and life cycle assessment of ammonia cofiring in coal power plants under the context of carbon neutrality. Energy Convers Manag. 2023;296:117648. doi:10.1016/j.enconman.2023.117648.
6. Siddiqui O, Dincer I. Design and analysis of a novel solar-wind based integrated energy system utilizing ammonia for energy storage. Energy Convers Manag. 2019;195:866–84. doi:10.1016/j.enconman.2019.05.001.
7. Li J, Chen S, Wu Y, Wang Q, Liu X, Qi L, et al. How to make better use of intermittent and variable energy? A review of wind and photovoltaic power consumption in China. Renew Sustain Energ Rev. 2021;137:110626. doi:10.1016/j.rser.2020.110626.
8. Kalaiselvan N, Mathimani T. Solar-driven green hydrogen generation for revolutionizing the future of zero-carbon energy. Fuel. 2024;375:132538. doi:10.1016/j.fuel.2024.132538.
9. Díaz-Motta A, Díaz-González F, Villa-Arrieta M. Energy sustainability assessment of offshore wind-powered ammonia. J Clean Prod. 2023;420:138419. doi:10.1016/j.jclepro.2023.138419.
10. Qi M, Kim M, Vo ND, Yin L, Liu Y, Park J, et al. Proposal and surrogate-based cost-optimal design of an innovative green ammonia and electricity co-production system via liquid air energy storage. Appl Energy. 2022;314:118965. doi:10.1016/j.apenergy.2022.118965.
11. Wen D, Aziz M. Techno-economic analyses of power-to-ammonia-to-power and biomass-to-ammonia-to-power pathways for carbon neutrality scenario. Appl Energy. 2022;319:119272. doi:10.1016/j.apenergy.2022.119272.
12. He J, Mao Z, Huang W, Zhang B, Xiao J, Zhang Z, et al. Low-carbon economic dispatch of virtual power plants considering the combined operation of oxygen-enriched combustion and power-to-ammonia. Sustainability. 2024;16(10):4026. doi:10.3390/su16104026.
13. Xu D, Zhou B, Wu Q, Chung CY, Li C, Huang S, et al. Integrated modelling and enhanced utilization of power-to-ammonia for high renewable penetrated multi-energy systems. IEEE Trans Power Syst. 2020;35(6):4769–80. doi:10.1109/TPWRS.2020.2989533.
14. Chen C, Liu D. Review of effects of zero-carbon fuel ammonia addition on soot formation in combustion. Renew Sustain Energ Rev. 2023;185:113640. doi:10.1016/j.rser.2023.113640.
15. Cai T, Zhao D, Gutmark E. Overview of fundamental kinetic mechanisms and emission mitigation in ammonia combustion. Chem Eng J. 2023;458:141391. doi:10.1016/j.cej.2023.141391.
16. Elbaz AM, Wang S, Guiberti TF, Roberts WL. Review on the recent advances on ammonia combustion from the fundamentals to the applications. Fuel Commun. 2022;10(1):100053. doi:10.1016/j.jfueco.2022.100053.
17. Sun W, Lin Q, Li H, Fang S, Chen Y, Cheng Y, et al. Simulation study on coal and ammonia cofiring in a tangential firing boiler under different ammonia injection methods. Sci Rep. 2025;15(1):15768. doi:10.1038/s41598-025-98792-5.
18. Wang G, Zhao J, Zhang H, Wang X, Qin H, Wu K, et al. Ammonia co-firing with coal: a review of the status and prospects. Energy Fuels. 2024;38(17):15861–86. doi:10.1021/acs.energyfuels.4c00872.
19. Yang L, Gao Y, Zhang P, Tan X, An J. Two-stage low-carbon economic dispatch of an integrated energy system considering flexible decoupling of electricity and heat on sides of source and load. Sustain Energy Grids Netw. 2024;40:101552. doi:10.1016/j.segan.2024.101552.
20. Liang J, Zhang G, Li F, Xie C, Wang T. Low-carbon optimal dispatch of integrated energy system considering hydrogen energy storage-ammonia production-carbon capture. Elect Power Automat Equip. 2024;44(10):16–23. (In Chinese). doi:10.16081/j.epae.202407009.
21. Fan H, Wang C, Liu L, Li X. Review of uncertainty modeling for optimal operation of integrated energy system. Front Energy Res. 2022;9:641337. doi:10.3389/fenrg.2021.641337.
22. Song H, Zhu G, Wang Z, Gao Y. Bi-level dispatch strategy for regional integrated energy systems considering multiple uncertainties and ammonia storage technology. SSRN. 2025. doi: 10.2139/ssrn.5147634.
23. Yang S, Wu H, Song J, Li H, Chen H. Two-stage robust optimization scheduling for integrated energy systems considering ammonia energy and waste heat utilization. Energy Convers Manag. 2024;319:118922. doi:10.1016/j.enconman.2024.118922.
24. Cao W, Wang S, Xu M. Optimal scheduling of virtual power plant based on Latin hypercube sampling and improved Clara clustering algorithm. Processes. 2022;10(11):2414. doi:10.3390/pr10112414.

25. Sharshir SW, Joseph A, Elsayad MM, Tareemi AA, Kandeal AW, Elkadeem MR. A review of recent advances in alkaline electrolyzer for green hydrogen production: performance improvement and applications. Int J Hydrogen Energy. 2024;49:458–88. doi:10.1016/j.ijhydene.2023.08.107.
26. Zhu Z, Lin J, Guo L, Han X. Multi-stage optimal scheduling of integrated energy system for independent island considering waste heat power generation and ammonia supply demand of power-to-ammonia system. Power Syst Technol. 2025. (In Chinese). doi:10.13335/j.1000-3673.pst.2025.0026.
27. Humphreys J, Lan R, Tao S. Development and recent progress on ammonia synthesis catalysts for Haber-Bosch process. Adv Energy Sustain Res. 2021;2(1):2000043. doi:10.1002/aesr.202000043.
28. Song J, Zhang Z, Mu Y, Wang X, Chen H, Pan Q, et al. Enhancing environmental sustainability via interval optimization for low-carbon economic dispatch in renewable energy power systems: leveraging the flexible cooperation of wind energy and carbon capture power plants. J Clean Prod. 2024;442:140937. doi:10.1016/j.jclepro.2024.140937.
29. Liu Z, Zhao J, Tao W, Ai Q. Optimization scheduling of combined heat-power–hydrogen supply virtual power plant based on stepped carbon trading mechanism. Electronics. 2024;13(23):4798. doi:10.3390/electronics13234798.
30. Chong Z, Yang L, Jiang Y, Zhou W. Hybrid-timescale optimal dispatch strategy for electricity and heat integrated energy system considering integrated demand response. Renew Energy. 2024;232:121123. doi:10.1016/j.renene.2024.121123.
31. Qi T, Hui H, Song Y. Chance constrained economic dispatch of central air conditionings in large-scale commercial buildings considering demand response. Energy Build. 2024;320:114607. doi:10.1016/j.enbuild.2024.114607.
32. Lu J, Hu J, Yu J, Chao J. Two-stage robust scheduling and real-time load control of community microgrid with multiple uncertainties. Int J Elect Power Energy Syst. 2024;155:109684. doi:10.1016/j.ijepes.2023.109684.
33. Zhao Z, Wu J, Wang B, Wang R. Research on source-load uncertainty optimal scheduling based on a hybrid robust multi-interval optimization method. Renew Energy. 2025;251:123316. doi:10.1016/j.renene.2025.123316.
34. Zhang X, Liu Y. Two-stage stochastic robust optimal scheduling of virtual power plant considering source load uncertainty. Eng Rep. 2024;6(12):e13005. doi:10.1002/eng2.13005.
35. Wang Z, Han Z, Zhao J, Wang W. Distributed robust scheduling optimization for energy system of steel industry considering prediction uncertainties. Inf Sci. 2024;666(4):120431. doi:10.1016/j.ins.2024.120431.
36. Liu X. Distributionally robust optimization scheduling of port energy system considering hydrogen production and ammonia synthesis. Heliyon. 2024;10(5):e27615. doi:10.1016/j.heliyon.2024.e27615.
37. Shi X, Xing H, Wang H, Mi Y, Huang C, Quan W, et al. Optimal scheduling of electricity-hydrogen–ammonia coupled integrated energy system based on uncertain renewable generations. J Renew Sustain Energy. 2025;17(3):034101. doi:10.1063/5.0246643.
38. Zhan Z, Xu J, Zhang T, Kong X, Li H, Zhang B. Optimal scheduling of integrated wind-photovoltaic-hydrogen energy system considering hydrogen application and waste heat recovery. Energy Rep. 2024;11:3684–94. doi:10.1016/j.egyr.2024.03.034.
39. Wang Y, Cheng X, Alhazmi M, Shi C, Xu M, Xie D, et al. Two-stage trigger dispatch strategy for hydrogen-electricity integrated station based on hybrid energy storage under response willingness uncertainty. J Energy Storage. 2025;116:116035. doi:10.1016/j.est.2025.116035.
40. Cui M, Liang X, Di Y, Niu F, Wang S. Study on the effect of ammonia mixing ratio on process of ammonia and coal co-combustion. J Energ Inst. 2025;120:102040. doi:10.1016/j.joei.2025.102040.